Chapter 21
Coherent EUV Light Sources Based on High-Order Harmonic Generation: Principles and Applications in Nanotechnology

Henry C. Kapteyn
Kapteyn-Murnane Laboratories Inc., Boulder, USA; and JILA and Department of Physics, University of Colorado at Boulder, USA

Margaret M. Murnane, Yuka Esashi, Michael D. Tanksalvala, Joshua L. Knobloch, and Chen-Ting Liao
JILA and STROBE NSF STC and Department of Physics, University of Colorado at Boulder, USA

Daniel D. Hickstein and Clayton Bargsten
Kapteyn-Murnane Laboratories Inc., Boulder, USA

Kevin Dorney and John Petersen
Imec, Leuven, Belgium

21.1 Introduction

Although the EUV lithography process makes good use of incoherent EUV illumination, many other applications—particularly in the area of metrology for nanotechnology, can either benefit from, or can only be done with, *coherent* light. In recent decades, a number of technologies have been developed to implement EUV sources that exhibit high spatial coherence: EUV lasers using highly ionized plasmas as the laser medium, short-wavelength free-electron lasers, and high-order harmonic generation (HHG). Of these technologies, HHG technology is both the smallest in scale and easiest to implement, and also exhibits the highest degree of coherence and control over the source characteristics. Furthermore, work in the past decade has proven the potential of these sources for nanotechnology applications in a variety of demonstration experiments. Thus, coherent HHG sources are poised to become an increasingly useful and valuable light source for metrology and imaging applications, in contrast to the high-power Sn plasma sources used for lithographic exposure.

In the HHG process, a femtosecond-duration laser pulse is focused into a collection of atoms or molecules (usually a gas, but liquid[2] and solid[3] materials have also been used) with a focal-spot intensity of $\sim 10^{13}$–10^{15} W cm^{-2}—an intensity sufficient to field-ionize these atoms. However, in contrast to plasma sources in which the target electron density is at or near the critical density where light no longer propagates into the medium, for HHG the free-electron density remains *underdense*, the laser continues to propagate, and the ionization process itself generates short-wavelength light. Because the HHG emission is directly driven by the laser field, high-energy photons are generated that are *phase coherent* with the driving laser. The basic physics of the process is shown in Fig. 21.1 and is often referred to as a *recollision* process. Ideally, each atom in the target is an isolated quantum system, with the electronic wave function of each atom responding deterministically to the same driving field. HHG occurs when the field is strong enough that the atom field ionizes. However, the atom and its parent ion remain an isolated, quantum-entangled system. The ionized electron does not immediately leave the vicinity of its parent ion, allowing its quantum wave function to interact coherently with the parent ion as it oscillates in response to the laser electric field. This results in a fully coherent electronic response that, when analyzed using quantum mechanics, reemits radiation at very high-order harmonics of the driving laser. In a classical picture, an electron ionizes, accelerates, and oscillates in response to the laser field, and can recollide

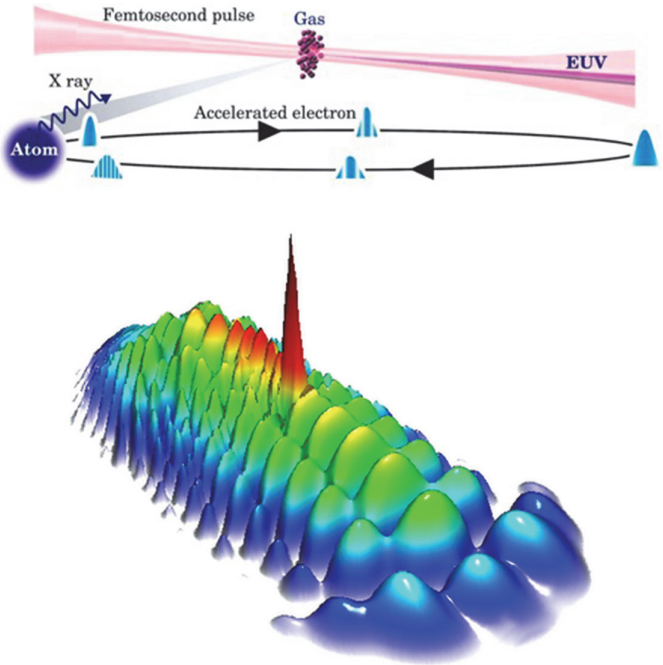

Figure 21.1 (top) Schematic of the HHG process. A femtosecond laser pulse is focused to intensities sufficient to field-ionize atoms in a gas. Once an electron is ionized, it begins to oscillate due to the electric field of the laser; in some cases, the ionized electron can re-encounter its parent ion and return to the quantum state from which it was ionized. To do this, it needs to lose its kinetic energy, which it does by emitting a high-energy photon. (bottom) Illustration showing a point in the evolution of the ionized electron's wave function. The re-encounter of the electron with its (charged) parent ion results in scattering and rapid oscillations in the electronic wave function. These rapid oscillations result in re-emission of EM radiation at photon energies corresponding to the kinetic energy of the electron oscillation, which is directly related to the intensity of the light. For near-IR ionization of rare-gas atoms, the intensity at the onset of tunneling ionization relates directly to emitted HHG photon energies in the EUV. (Top figure reprinted from Ref. 1.)

with the parent ion (Fig. 21.1) with considerable kinetic energy; this classical picture yields a remarkably accurate estimation of the range of photon energies that can be generated.[4] The electrons that recombine with the ion must give up their kinetic energy as they abruptly stop.

In this way, the HHG process corresponds to a coherent version of the Röntgen x-ray tube, where electrons are extracted from a filament, accelerated in a field, and then collide with a target to produce x rays. In HHG, electrons are coherently extracted from a well-defined coherent state of an atom, are accelerated, and then collide with a target *with which the electron is indeed still coherent.* The HHG process relies on the quantum entanglement of the electron–ion "system" created by the strong-field ionization.

Although the intensities required for ionization—10^{13} to 10^{15} W cm^{-2}—are quite high, they are routinely accessible with tabletop-scale femtosecond lasers. This gives us the ability for the first time to implement a tabletop-scale x-ray laser, in the same sense that many of the green, blue, and ultraviolet lasers in use in science and industry are also upconverted infrared lasers.[5] The ability to upconvert, in a single conversion step, from the IR/VIS into the VUV, EUV, and even soft-x-ray regions of the spectrum not only allows for the small-scale implementation of many analytical, microscopy, and metrology techniques first developed at synchrotrons, but also makes possible new studies of ultrafast dynamics and pump–probe characterization. Furthermore, since HHG is a coherent upconversion process, it is possible to control the characteristics (wavelength, chirp, polarization, orbital angular momentum) of the laser, and have this coherent manipulation translate into controlled coherent characteristics of the EUV light. Since the dynamics of the process is sub-optical-cycle in nature, HHG corresponds to the first complex, non-trivial *attosecond* process to be studied, and to potentially be useful.

High-harmonic emission in the extreme ultraviolet was first observed in 1987,[6] preceded by experimental work by some of the same authors who observed high harmonics driven by a CO_2 laser.[7] Subsequent work clearly demonstrated the *non-perturbative* nature of the laser–atom interaction, with a large number of harmonic orders of similar conversion efficiency, followed by a relatively abrupt cutoff photon energy.[8] The basic mechanism for HHG was first understood through quantum numeric simulations,[9] in which a key realization was the need to increase the physical size of the simulation to be considerably larger than the size of the atom and of the oscillation of the newly ionized electron. The simulations then revealed a cutoff energy of $h\nu_{\text{cutoff}} \sim 3U_{\text{p}}$, where

$$U_{\text{p}} = \frac{e^2 I}{2c\varepsilon_0 m\omega_0^2} = \frac{2e^2}{c\varepsilon_0 m} \times \frac{I}{4\omega_0^2} \tag{21.1}$$

is the mean oscillation energy (ponderomotive energy) of a free electron in a laser field.[10]

The most pivotal experimental enabler both for purposes of experimentally corroborating the physics of HHG, and for its practical application, has been the development of lasers capable of generating intense *few-cycle* (i.e., $<\sim$10 cycle) light pulses. The HHG process happens in a dynamically changing environment, where the medium generating the HHG radiation is rapidly being destroyed. Reaching the requisite intensity as quickly as possible allows for generation of HHG light at higher intensities. Figure 21.2 shows examples of the high-harmonic spectrum obtained using few-cycle driving lasers.

The laser material titanium-doped sapphire was developed in the 1980s[13] and has an extraordinarily large spectral gain bandwidth of nearly 0.5 eV,

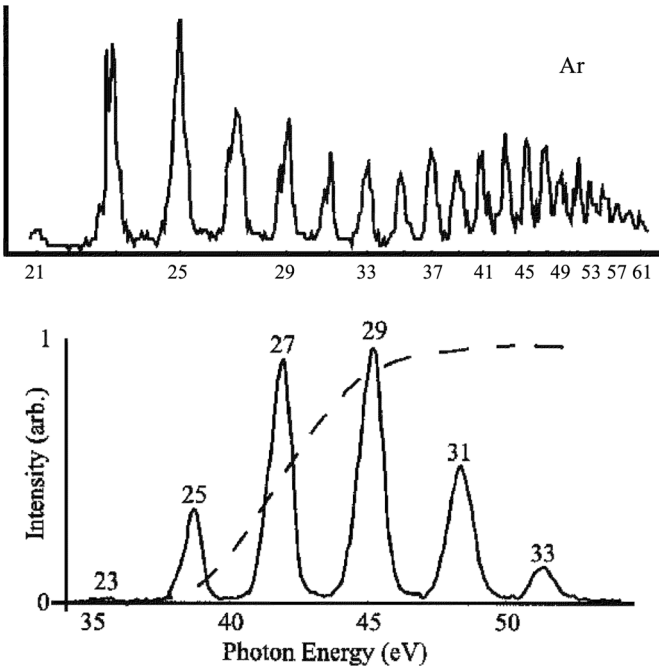

Figure 21.2 Examples of high-order harmonic spectra emitted by low-pressure argon gas driven by a Ti:sapphire laser focused to an intensity of $\sim 10^{14}$ W-cm^{-2}. (top) The first example of HHG driven with a few-cycle (25 fs, ~9 optical cycles) laser pulse incident into a very low-pressure gas, showing a *cutoff harmonic order* of 61 (13 nm). (bottom) Spectrum when the flux is fully optimized, with much brighter (~1000x) emission but with a lower energy *phase-matching cutoff*. Dashed line corresponds to the transmissivity of the argon gas, illustrating that the spectrum coincides with a window in the EUV absorption of argon, allowing for higher pressure (and thus higher flux). (Top figure reprinted from Ref. 11; bottom figure reprinted from Ref. 12.)

which (through the $\Delta E \Delta t$ relationship) means that it is capable of both generating near-single-cycle light pulses and amplifying few-cycle light pulses.[14] This capability opens a new regime of light–matter interactions with an optical field whose amplitude and frequency are changing significantly on a cycle-by-cycle basis. This property, in turn, makes it possible to see the quantum dynamics of HHG directly in the spectrum of the emission; Fig. 21.3 shows examples of this. With a few-cycle pulse, the relative phase and timing resulting from the recollision varies from cycle to cycle, leading to changes in the spectrum as the *chirp* (optical phase) of the driving laser is varied. This variation can be modeled through quantum simulation,[15] and these physics can further be used to *control* the spectrum.[16] These experiments are the first examples of *attosecond science*, exploring nontrivial dynamics on the shortest timescales.

The few-cycle lasers used in the work that resulted in Figs. 21.2 and 21.3, and which are still central to practical implementation of HHG, resulted from

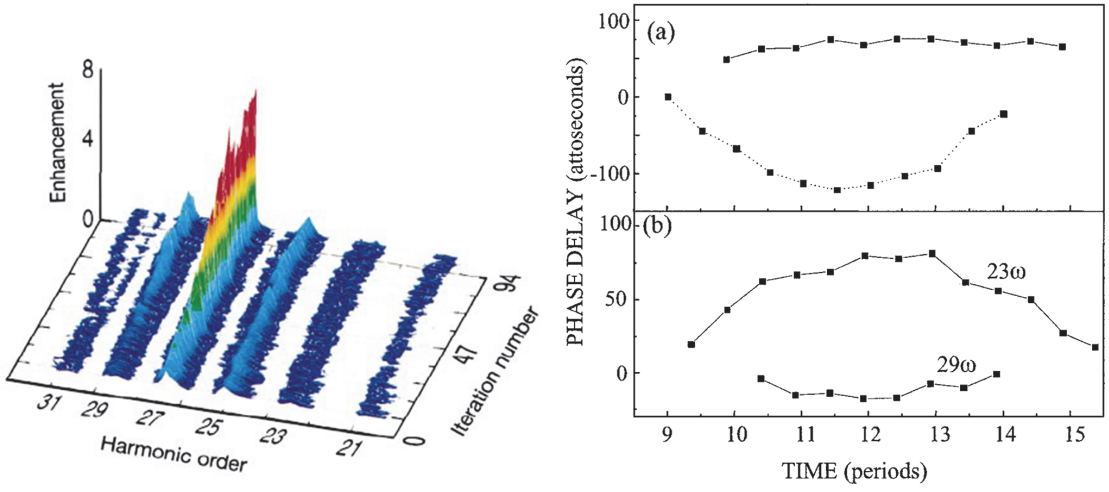

Figure 21.3 The effect of chirp and pulse shape on the spectrum of HHG emission, as a directly observable manifestation of the recollision process in HHG. In a conventional nonlinear optical process (where the nonlinear response is instantaneous), a Fourier-transform-limited pulse would result in the strongest signal at all given wavelengths. However, this is not the case for HHG—it is unique as a *purely electronic* NLO process with a non-instantaneous response resulting from the recollision mechanism of Fig 21.1. In the experiment above, a pulse shaper was used to fine-tune the exact cycle-by-cycle oscillations of the driving laser pulse. HHG emission consists of a series of attosecond-duration broad-bandwidth bursts, whose coherence and periodicity result in interferences that result in the individual spectral peaks of HHG. However, the **phase** of this emission at any particular frequency is not fixed with respect to the phase of the laser oscillations driving the HHG process, since the timing of the recollision process with respect to the peak of the pulse varies with intensity, resulting in an *intrinsic phase* of HHG.[26] Introducing a nonlinear chirp to the pulse makes it possible to adjust the timing of each burst by essentially varying the instantaneous frequency of the driving laser. The result is that constructive interfererence of **a selected** harmonic order can result in enhancement. (left) In this work, the laser started with a time-bandwidth-limited pulse at iteration 0. By adjusting the pulse shape, an order-of-magnitude increase in the spectral brightness for H27 in Ar gas was obtained. (right) Schematic illustration of this optimization, showing the timing shifts required for optimization of different harmonic orders. This represents the first demonstrated application of *attosecond physics*, alongside prior experiments that demonstrated the coupling of spectrum to optical phase.[15] (Left figure reprinted from Ref. 16; right figure reprinted from Ref. 27.)

a series of rapid interrelated technology developments: the demonstration of mode-locked Ti:sapphire lasers,[17] chirped pulse amplification,[18] and a deeper understanding of, and control over, dispersion in both mode locking[19,20] and ultrafast-laser-amplifier systems.[14,21] These technologies converged rapidly, with HHG among the first applications. Their utility immediately became apparent through the higher harmonic orders and higher conversion efficiency observed,[11] and through quantitative verification of the $I_p + 3.17\ U_p$ cutoff rule.[22,23]

These few-cycle lasers were also critical in understanding the dynamic mechanism behind *phase matching* of the HHG process. Phase matching is the basis for nonlinear optics.[24,25] It corresponds to the case in nonlinear frequency conversion when emitters over an *extended* region of a material all emit constructively to generate a forward-directed beam. In conventional NLO, this is accomplished through ensuring that the index of refraction of the pump light and the (nonlinear) signal light are the same—generally by using crystal birefringence. However, in HHG, phase matching is fundamentally different. In HHG, as the atoms ionize, the index of refraction of the gas for the driving laser changes—an electron bound in an atom contributes a positive value to the refractive index, while a free-electron plasma contributes a negative value. Since the magnitude of the free-electron refractive index is generally greater, there is a *critical ionization value* at which the two contributions balance and the phase velocity is **c**. Since the phase velocity of the harmonics themselves is very near **c**, phase matching is, *in general*, possible in a partially ionized medium, and it is a *dynamic* process.

This dynamic nature has numerous implications distinct from conventional nonlinear effects—for example, the time duration of the HHG emission is generally shorter than that of the driving laser, while in conventional NLO for femtosecond pulses, it is generally longer due to spectral narrowing. However, from an implementation point of view, the most important implication is that the ionization of the medium constrains the usable peak intensity of the driving laser. Once the medium is ionized past its critical ionization value, fully phase-matched emission is no longer possible. Thus, the HHG process is extremely sensitive to the rise-time of the driving laser pulse, but in a way that does not scale simply—conversion efficiency to a particular wavelength increases rapidly with shorter pulse duration until this particular wavelength is generated at a level of ionization that is below critical. Even shorter pulses serve to increase the cutoff photon energy without dramatically increasing the conversion efficiency to any particular wavelength.

Phase matching of HHG was first revealed using a few-cycle pulse, in the case where the laser and the gas were both confined within a waveguide.[28] The waveguide adds a pressure-independent factor to the phase-matching expression, allowing for gas pressure-dependent control of the phase-matching conditions. This allowed for the observation of a sharp and clear pressure

optimization, which clearly revealed the mechanism behind HHG phase matching. In the absence of a waveguide, the phase-matching condition is determined only by the fractional ionization, which is generally not measurable.

21.2 Practical Implementation of HHG

Implementation of a HHG light source is, in principle, simple: one needs a laser capable of focusing to the intensity required by the cutoff relation, and one needs a medium to focus the light into, which will be ionized. However, the physics of the process dictates a number of other requirements for optimized conversion efficiency:

1. The focused beam should ionize the gas to the critical ionization level for phase matching at the time of the *peak* of the laser pulse.[12,28] The optimal intensity and the characteristics of the harmonic spectrum depend on the medium, and the laser pulse shape and duration. *Overdriving* the medium generally degrades the efficiency and beam quality (though the flux may still increase due to larger mode area), without substantially increasing the observed cutoff photon energy.
2. The conditions above set the cutoff photon energy for phase-matched harmonic generation. The usable spectrum is in the range of 0.5–0.9 $h\nu_{\text{cutoff}}$. If the desired photon energy is not in this range, either the nonlinear medium or the driving laser characteristics must be adjusted. Figure 21.4 shows the dependence of $h\nu_{\text{cutoff}}$ on laser wavelength, in the case of a pulse 8 optical cycles FWHM duration and for the noble gases. Using the shortest possible driver laser wavelength generally optimizes conversion efficiency as the effective nonlinearity of the HHG process decreases rapidly with increasing wavelength.[29]
3. The focus region must sustain this intensity over a length corresponding to several XUV/soft x-ray absorption lengths of the generated light.[30,31] This allows for build-up of the HHG intensity to a value limited by the reabsorption of the signal light.
4. The region of dense gas must end as abruptly as possible after the focus of the beam before the laser intensity decreases significantly. If this is not the case, the HHG cutoff recedes, shutting-off emission but not re-absorption. This places a lower limit on the useful peak power of the laser: the confocal parameter (i.e., length of focus) of beam should generally be significantly longer than the entire region where gas pressure is significant.
5. Generally, except in special cases, the highest HHG efficiency is obtained by using the shortest laser wavelength where the desired $h\nu_{\text{cutoff}}$ is reached. The "single atom" nonlinear response during the recollision process falls rapidly using longer-wavelengths to drive the HHG process.

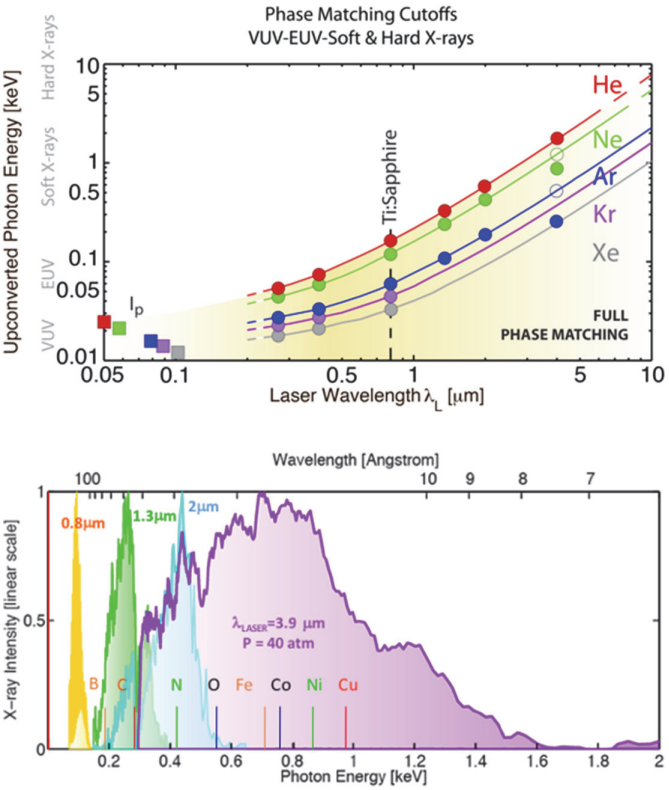

Figure 21.4 Phase-matched HHG: experiment confirms predictions that using longer-wavelength driving lasers produces phase-matched emission to shorter wavelengths for fully phase-matched HHG in weakly ionized gases. Further experimentation and theory may reveal new regimes of efficient HHG; see, e.g., Ref. 33. (top) Phase-matching cutoff for a pulse of 8 cycles duration as a function of the driving laser wavelength and for various gas media. (bottom) Experimental data showing HGG spectra using helium gas and driving laser wavelengths of 0.8 μm, 1.3 μm, 2 μm, and 3.9 μm, validating the predictions of the top graph (Reprinted from Ref. 32.)

These conditions set a narrow optimum parameter range that—depending on the gas and laser wavelength—results in conversion efficiency approaching 10^{-3} for UV laser upconversion into the VUV, decreasing slowly to $<\sim 10^{-7}$ for soft-x-ray generation using mid-IR lasers. The ultimate limit to the coherent photon energy that could be generated using HHG is not known. In fact, simple models predict that the conversion efficiency of laser light to coherent x rays may actually increase when using even longer-wavelength lasers to drive the process.[34] However, the requisite laser technology must be developed.

Phase matching of HHG is a general property of the process regardless of the particular focusing geometry implemented; however, the ability to obtain optimal conversion efficiency varies with geometry. The first HHG experiments

used a pulsed valve to create a confined region of gas; however, this geometry is difficult to optimize, inefficient in use of gas, and limited in pressure achievable at the target. Gas cell geometries, where the laser exits through a differential pumping pinhole, create the required abrupt gas–vacuum interface; this cell can either be *semi-infinite* with the beam focusing in the gas,[35] or can be confined by an entrance as well as an exit aperture. The entrance aperture is essential if nonlinear effects of the beam on the way to the focus degrade the focus or create instabilities, which is often the case.

Confining the gas within a hollow capillary waveguide with holes drilled in the side for gas inlet allows for careful control over the gas pressure profile while also guiding the laser using total external reflection and extending the useful interaction length. Waveguides also minimize gas usage since the gas flow is coincident with the propagation aperture of the laser, and the extended propagation length can also optimize the spatial coherence.[36] The relative benefit of using a waveguide varies. Generally, for VUV–XUV high harmonics using gases such as xenon and krypton, re-absorption of the HHG is quite strong, while the required laser intensity is relatively low, both of which allow for optimization using a thin low-pressure gas cell. For HHG in argon gas, a minimum in EUV absorption around 50 eV/25 nm permits an extended interaction length, allowing for clear phase-matching in a waveguide.[28] For generation of light at $h\nu > \sim 100$ eV, the waveguide geometry becomes increasingly advantageous. The optimum driving-laser wavelength increases (the basic high-harmonic cutoff relationship makes this clear: $h\nu_{\mathrm{cutoff}} = I_{\mathrm{p}} + 3.17\ U_{\mathrm{p}} \sim \propto I\lambda^2$), making tight focusing more difficult due to diffraction, and guiding more desirable. Simultaneously, the optimum gas density-length product rapidly increases with decreasing HHG wavelength, making gas handling impractical in all but a waveguide geometry. Using a waveguide with a gas target pressure of $>\sim$10 atm helium, and a mid-IR 3.9-μm driving laser, a coherent spectrum spanning to >1 keV can be generated (Fig. 21.4).

When all of these factors are considered, we can add another, somewhat more, tentative conclusion for optimization of HHG:

6. Except in limited cases, or when the laser wavelength is fixed and use of a different gas suitably (down) shifts the harmonic cutoff, helium gas appears to be the most efficient HHG nonlinear medium. Inner-shell absorption in other species represents an incoherent loss mechanism, while (with no inner-shell absorption) helium becomes transparent into the x-ray spectral region. Atomic hydrogen might work even better were it practical to use at high pressures. Molecular hydrogen and other non-centrosymmetric molecules, in general, exhibit lower efficiency because the HHG phase can vary with orientation.

This outlook is somewhat contrary to the prior "conventional wisdom" for HHG, which previously saw very weak or no emission from helium gas in

conventional gas-jet geometries, and concluded that it was a poor choice for HHG. Optimization of HHG in helium gas requires much higher pressures than are generally possible in simple gas-jet or even cell geometries, explaining this misperception. The absorption and HHG emission processes are quantitatively linked,[37] and cannot be considered in isolation to estimate HHG efficiency. The exact relationship of conversion efficiency to gas medium is still an area of considerable uncertainty since experimental phase-matching conditions vary and can only be approximately known. An educated guess—consistent with our observations to date—is that coherent HHG emission is exclusively due to ionization of the outermost shell, with similar emission per ionized electron, but where the generated light can be re-absorbed by any electron that can be ionized. For example, for neon with a $1s^2 2s^2 2p^6$ configuration, 6 electrons participate in emission, while for $\lambda = 13.5$ nm ($h\nu = 92$ eV), 8 electrons can re-absorb this light. Thus, neon might be expected to be less efficient in this spectral region compared with helium, where both electrons are identical—given that all other parameters are optimized for each gas. The effect of inner-shell absorption on suppressing HHG efficiency is clearly seen in the case of argon soft-x-ray emission using mid-IR driving lasers.[32]

Finally, it is also important to point out the possibility of further breakthroughs in increasing conversion efficiency. For example, quasi–phase matching can be implemented with HHG, with the most-versatile scheme simply shutting off HHG using a counterpropagating laser pulse.[38–41] Another regime of HHG recently revisited is the use of short-wavelength, UV driving lasers.[33] The simple picture of phase matching described previously assumes that the refractive index of the ions can be neglected. This assumption is increasingly inaccurate with short-wavelength drivers: the index of refraction of the neutral gas is higher, the negative contribution due to the field-ionized plasma is smaller, and the contribution of the ions to the total optical index of refraction is greater. All of these factors diminish the effect of phase mismatch. High-harmonic light up to the water window region of the spectrum has been observed using UV drivers.[33] However, this approach is not without its challenges in maintaining a reasonably short-duration UV pulse simultaneous with a high beam quality. Thus, these more experimentally complex approaches remain *experimental*.

21.3 HHG for Generating Coherent 13.5-nm EUV Light

Following the guidance of the previous section, excellent conversion efficiency to $\lambda = 13.5$ nm ($h\nu = 92$ eV) can be obtained under conditions of:

1. Helium as a gas target (neon may in some cases be useful as lower pressures are required—but it is also much more expensive to use).
2. Driving laser pulse at $\lambda \sim 800$ nm, $\tau \sim 20$–40 fs.
3. Target pressure up to $\sim$1 atm.

The graph of Fig. 21.4 shows a cutoff photon energy for these parameters, of ~130–150 eV, which sets the peak of emission very near the 59th harmonic of 796 nm = 13.5 nm. Ultrashort-pulse Ti:sapphire laser drivers are thus an excellent driving laser for efficient HHG to 13.5 nm. Figure 21.5 shows typical spectra from the commercialized HHG source of Fig. 21.7 [the Kapteyn-Murnane Laboratories Inc. (KMLabs) RAEA™ ultrafast Ti:sapphire laser amplifier and XUUS™ high-harmonic system].

21.3.1 Characterization of HHG sources

Flux characterization of HHG sources is challenging and can be error-prone if not done carefully. The HHG light has a spectrum that spans from the wavelength of the infrared driving laser all the way to the EUV/SXR region of the spectrum, with only a very small fraction of this light at any particular desired wavelength. Multiple checks must be done to ensure that the measured signal is not originating from out-of-band (OOB) radiation, i.e., either the driving laser light itself *or lower-order harmonics of the laser* such as 3ω or 5ω (where the total photon numbers can significantly exceed the EUV flux).

Generally, EUV light is separated from these other harmonics using a multi-stage process. After the light leaves the generation region, it is co-propagating with a much brighter driving laser beam. The bulk of this energy is best removed from the beam using reflective optics. For photon energies <~50 eV, a silicon substrate placed at Brewster's angle for the 800-nm can absorb the incident laser light and be highly reflective for the EUV light.[42,43] For shorter wavelengths such as 13.5 nm, and to avoid thermal loading of these rejector mirrors, specialty coatings and transparent substrates can be used in a similar way to reflect the EUV and transmit the 800 nm.

Once >~90–99% of the incident light is rejected from the beam, the remaining laser light and lower harmonics can be blocked using thin metal filters. For $h\nu < 70$ eV, aluminum filters in the range of 0.1- to 0.5-μm thickness have proven to be very robust. However, for 13.5 nm, Zr filters have proven most useful for isolating the harmonic of interest. More than one filter must be used in the beam for accurate flux measurement, as pinholes and other leak-through from a single filter can create a background.

The setup of Fig. 21.6 illustrates the resulting setup for calibrated flux measurement. Following the HHG source, two reflective rejectors separate the bulk of the laser light from the EUV. This is followed by 3 thin metal filters—Zr for measuring the spectrum near 13.5 nm. By using three filters, any two of them can block the OOB radiation, and the third can be moved in and out to calibrate the transmission characteristics of each filter. These filters can degrade quickly from oxidation; therefore, an inline characterization setup is necessary. In our setup, we then use either an EUV silicon diode (quantum efficiency specs in data sheet),[44] or a NIST-calibrated

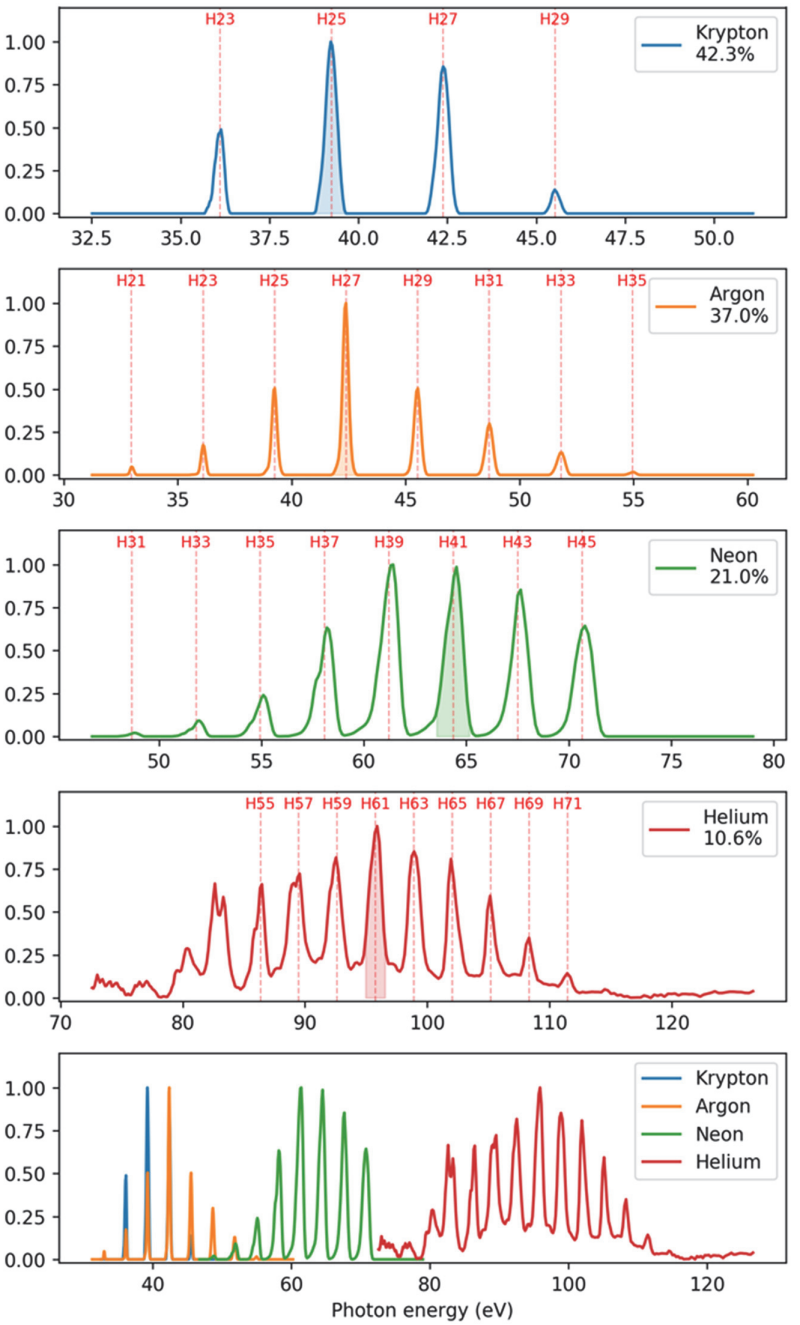

Figure 21.5 Example experimental HHG spectra obtained from a KMLabs RAEA™/XUUS™ HHG system, illustrating real-world spectral ranges for HHG using Ti:sapphire lasers. Note that the spectra are modified by the thin-film metal filters used: aluminum for Kr, Ar, and Ne HHG; Zr for helium HHG. Specifically, harmonics with $h\nu < 20$ eV and >72 eV are blocked by the thin-film aluminum filter.

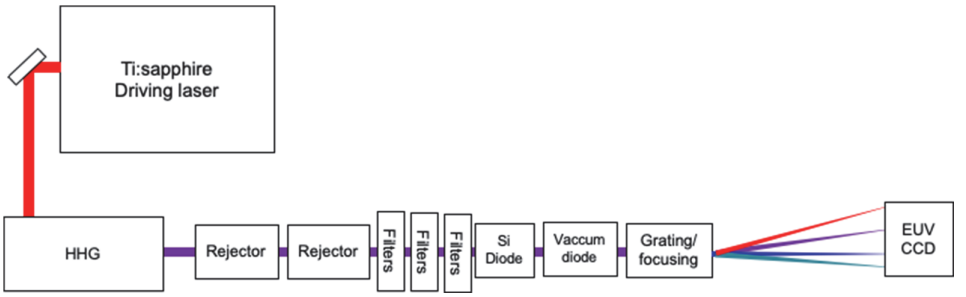

Figure 21.6 HHG setup for reliable HHG source flux characterization. The driving laser is focused into a gas, in a variety of possible interaction geometries. Following HHG, a pair of reflective rejectors transmit the driving laser light and reflect VUV–EUV wavelengths. Following the rejectors, three removable/insertable filters allow for further rejection of the co-propagating out-of-band radiation. At this point, insertable silicon and vacuum photodiodes can be used to characterize the total in-band flux. Finally, a grating spectrometer and EUV-sensitive CCD camera can be used to characterize the spectrum of this radiation.

visible-blind Al_2O_3 vacuum photodiode.[45] The measured photodiode current then characterizes flux of the emission spectrum incident on the detector.

To verify that this light is indeed in-band radiation, a number of checks must also be performed. First, shutting off the gas flow to the HHG should result in the signal dropping to zero—if not, some of the driving laser light is being detected by the photodiode. Next, any leak-through of the lowest harmonics 3ω, 5ω, and 7ω must be characterized, as the attenuation of Zr filters at these wavelengths can be incomplete; particularly for the case of using a Si photodiode, a total attenuation of OOB radiation of $\sim 10^{12}$–10^{15} is required.

Checking for OOB radiation is done through a combination of checks. First, a LiF or MgF_2 window is an effective low-pass filter to block any photon energies $>\sim 10$ eV. Second, decreasing the driving laser intensity, or introducing a small amount of ellipticity into the beam by adjusting a waveplate, will affect the EUV generation more rapidly than it quenches any VUV background. If the signal drops to zero with small decreases in energy or increases in ellipticity, this is a good indicator of a clean in-band EUV signal.

Finally, a grating spectrometer can be used to determine the spectrum of emission corresponding to the measured currents. Provided that the grating diffraction efficiency does not vary dramatically over the observed spectrum of emission, the fraction of the measured spectrum that is in the (narrower) region of interest (e.g., 13.5 nm) can be determined. The spectrally resolved transmission characteristics of each of the filters can also be characterized more accurately by taking out one of the three filters at a time and measuring the spectrum with and without that filter. The reflectance characteristics of the rejectors are more difficult to characterize, as inserting a third rejector changes the beam path and requires its reconfiguration. However, generally, if this

optic is visibly clean, our measurements have found the reflectance to be high (~70%) for a design appropriate for the desired wavelength band—a value that is close to that predicted by calculations.[46] The high overall efficiency results in a relatively small contribution to error in source flux estimates. Generally, these rejectors always remain in place, while the filters may not be necessary for any particular experimental application.

It is tempting to determine source flux directly from count rates on a CCD camera; however, we have found that this method generally results in significant overestimates if not cross-calibrated carefully with the method previously described. This can be due to a number of factors: the CCD can accumulate exposure even during readout, calibrations of CCD A/D conversion may be inaccurate, or the thickness of the passivation layer on the CCD may be variable, resulting in variable attenuation of EUV (but no effect on IR/Vis). However, the CCD does have an advantage in making longer-wavelength scattered light apparent in the CCD image. In any case, flux measurement is difficult enough that for truly reliable numbers, multiple methods should be used and should give reasonably consistent results.

Other HHG source characteristics that are critical to precision applications of the source include the overall flux stability (both short term and long term), mode quality, and the pointing and positional stability of the source. Flux degradation can occur due to creeping misalignment, laser instabilities, and contamination of the optics; in particular, the reflective rejectors and any filters cannot be placed too close to the source. Mode quality depends on alignment as well as the phase-matching conditions of the light source,[47] but can be nearly Gaussian in shape when it is well–phase matched and focusable to near (i.e. within ~2×) the diffraction limit.[48] Finally, we have found that routine use of the light source depends on excellent positional stability of the source—typical focal spot sizes for the re-focused HHG light can be just a few microns so that any pump–probe or interference experiments that rely on spot overlap rely on sub-μm/μrad stability of the source. A positionally stable source often requires active driving laser beam-pointing adjustment, as well as mitigation of any nonlinearities in delivery of the ultrashort-pulse beam to the HHG interaction region, and meticulous consideration of thermal loads that may deflect or distort an optic and cause beam wander. HHG is most likely the most-demanding application of ultrafast lasers to date, with many potential pitfalls.

21.3.2 Example characterization of a commercial HHG source

Commercialization of HHG sources, and previous to this the first commercialization of the requisite few-cycle, high-power sub-terawatt Ti: sapphire lasers, has been pioneered by KMLabs.[49] A second company employs a scheme similar to KMLabs,[50] and a third company is selling a fiber-laser-based source primarily for lower-photon-energy HHG.[51]

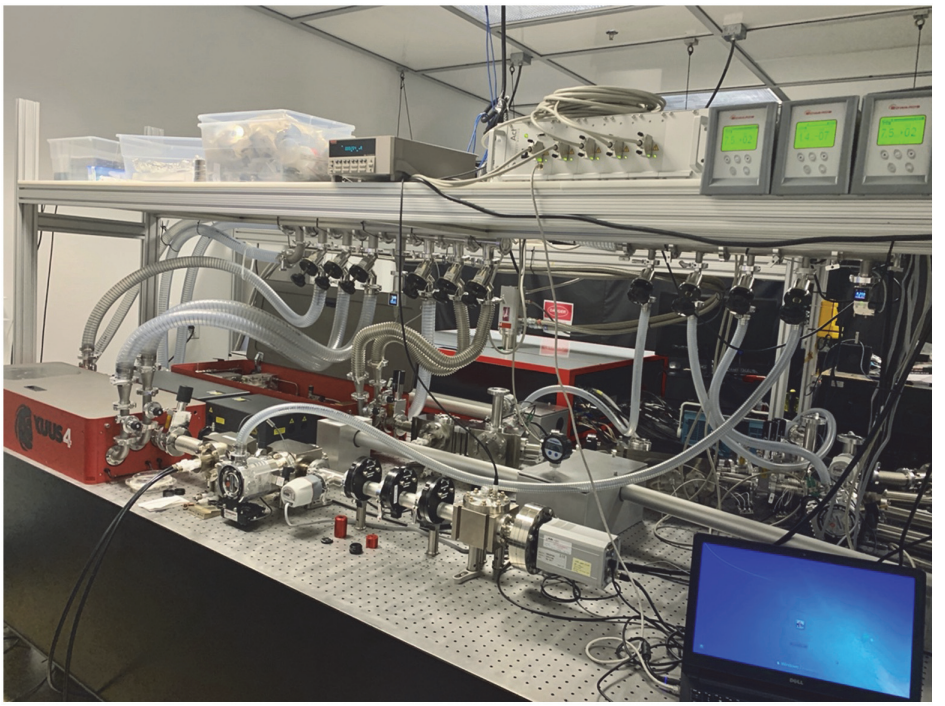

Figure 21.7 Photograph of a HHG light source and beamline for generation of light at $\lambda = 13.5$-nm and longer wavelengths. In this photo, the driving laser, a KMLabs RAEA™, is at the back. Two separate XUUS4™ HHG systems are visible on the front table, with a characterization beamline at the front.

Figure 21.7 shows a typical setup of the KMLabs RAEA™ ultrafast Ti:sapphire laser, along with KMLabs XUUS4™ HHG source, and a beamline configuration for flux characterization as well as experimental applications. KMLabs uses a modular beamline approach that can be reconfigured for a variety of purposes. We have evaluated other manufacturers' lasers with the XUUS, and find comparable HHG photon numbers *per pulse*, with the overall flux correspondingly lower in proportion to their lower (1 kHz) repetition rate. For any given focal geometry for HHG, the emission will saturate at a given pulse energy, beyond which the flux increase is marginal and the HHG beam quality degrades. The RAEA™ laser uses an aggressively cooled laser medium, which provides the unique capability to run at high- ($\sim$2–3 mJ) energy and multi-kilohertz repetition rates, with the ability to trade off pulse energy with repetition rate. Thus, the optimum pulse energy of the laser can be determined directly through HHG flux, with the repetition rate then increased to fully utilize the output power of the driving laser. Table 21.1 presents basic system parameters and flux measurements from a setup corresponding to Fig. 21.6. Figure 21.8 shows long-term flux stability measurements, along with the full spectrum obtained

Table 21.1 Essential parameters and flux measurements for the HGG source in Fig. 21.7. (FROG is frequency-resolved optical grating; BW is bandwidth.)

Parameters	
Laser source	KMLabs RAEA™ HP-SP+
Pulse duration measured using FROG	24 fs
Pulse repetition rate	5 kHz
Laser output power as used	11 W
Characterization photodiode type	Al_2O_3 photoemission diode
Photodiode responsivity @13.5 nm (A/W, NIST)	9.36×10^{-4}
Gas type, pressure	helium, 500 Torr
Rejector #1 reflectance (CXRO) @ 13.5 nm	
Rejector #1 reflectance (measured) @ 13.5 nm	90%
Rejector #2 reflectance (CXRO) @ 13.5 nm	86%
Rejector #2 reflectance (measured) @ 13.5 nm	90%
Filter #1 type, thickness	Zr 0.2 μm
Filter #1 transmission (CXRO) @ 13.5 nm	50%
Filter #1 transmission (measured avg. over band)	30%
Filter #2 type, thickness	Zr 0.2 μm
Filter #2 transmission (CXRO) @ 13.5 nm	50%
Filter #2 transmission (measured avg. over band)	28.2%
Calculations	
Average photodiode current (full spectrum)	157 pA
Flux at detector (full spectrum, filters #1 and #2)	1.14×10^{10} ph/sec
Flux after rejectors (full spectrum)	1.35×10^{11} ph/sec
Est. flux @ source (full spectrum)	1.66×10^{11} ph/sec (~3 μW)
Fraction of flux @ 13.5-nm harmonic (~1 eV BW)	6% (red-highlighted peak)
Total flux in single harmonic order @13.5 nm	1.0×10^{10} ph/sec (0.15 μW)
Spectral bandwidth of a single harmonic	~0.5 eV

from this setup, and used to estimate the fraction of flux in the spectral peak corresponding to 13.5 nm.

21.3.3 Alternatives to Ti:sapphire lasers for $\lambda = 13.5$ nm

An alternative for 13.5-nm HHG is to use lasers at 1-μm wavelength. For example, compared to Ti:sapphire lasers, ultrafast Yb:fiber lasers operating at ~1.03–1.06 μm are much more efficient at generating ultrafast laser pulses and have been scaled to kilowatt power levels. Unfortunately, this technology cannot directly generate pulses with few-cycle duration because the limited bandwidth of the medium sets a lower limit of pulse duration at <~200 fs, with more typical pulse durations of 300–800 fs. Note that this limitation is intrinsic to the higher efficiency of the Yb–laser transition, which results from

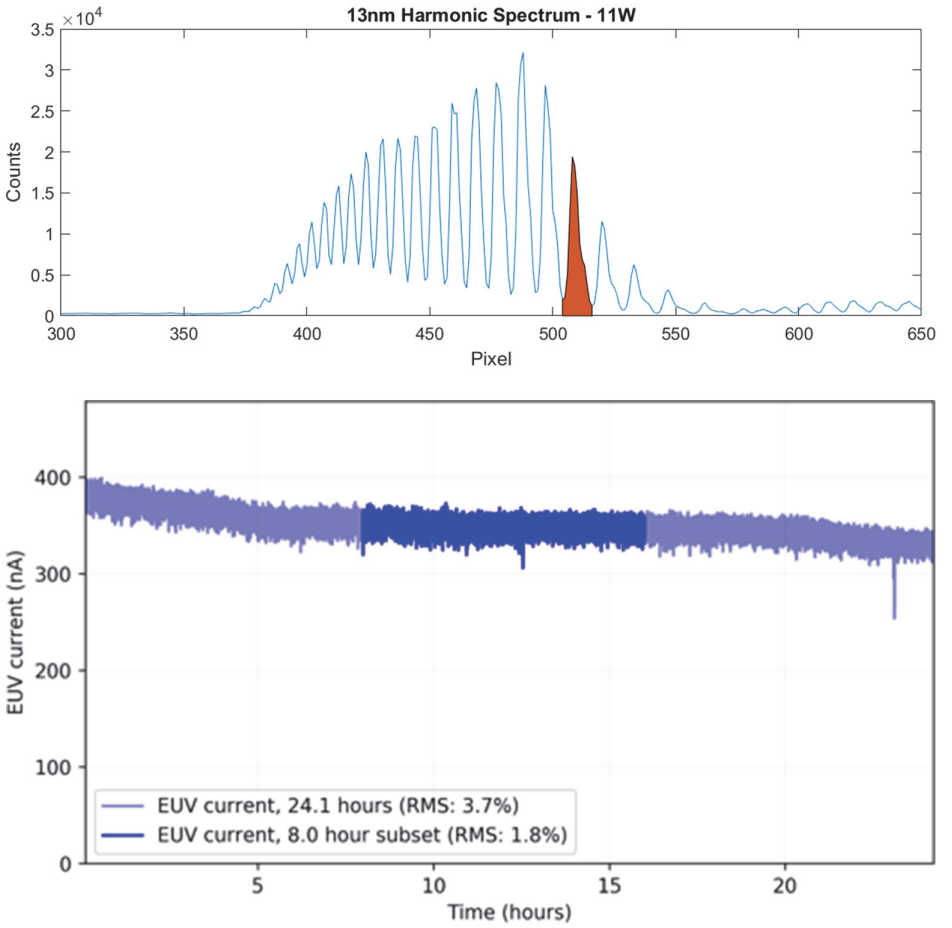

Figure 21.8 Additional characterization data corresponding to the setup of Table 21.1. (top) Harmonic spectrum plotted with higher photon energies to the left, with 92 eV (13.5 nm) highlighted. The spectrum extends to ~140 eV in this case. (bottom) Long-term stability data. Here, the higher current than quoted in Table 21.1 is the result of using a silicon photodiode rather than an Al_2O_3 vacuum diode.

a low quantum defect in the laser medium and thus necessarily a narrower gain bandwidth and longer intrinsic pulse duration.

Driving HHG with a ~100-optical-cycle pulse not only requires a proportionately higher pulse energy to obtain the same peak intensity, but also results in much more ionization as the pulse intensity increases to that required to bring the cutoff photon energy up to that corresponding to the harmonic of interest ($\sim 77^{\text{th}}$ harmonic of 1040 nm for 13.5 nm). This significantly lowers the phase-matching cutoff photon energy. Furthermore, the sub-millijoule pulse energies available from a single fiber laser amplifier would require an extremely tight focus, a short confocal parameter, and a higher optimal pressure, and would lead to exponentially more difficult

problems in confining the gas target to the focus region. Thus, this direct approach is limited to wavelengths longer than 13.5 nm.

Attempts to bypass this limitation involve either (1) operating several fiber channels in parallel and then coherently combining the outputs; (2) use of nonlinear pulse compression techniques to reduce pulse duration to 30–50 fs, in one stage of nonlinear pulse compression, or to ~10 fs in two stages, or (3) both. The first approach would still suffer from a limited phase-matching cutoff energy. The second approach can be employed for $\lambda = 13.5$ nm; however, nonlinear pulse compression also typically results in significant degradation in both the temporal pulse quality (i.e., although there may be a "spike" in peak power of the short, compressed pulse, this spike contains only a fraction of the energy that would be measured with a power meter) *as well as* the focusability of the pulse. Unfortunately, published works on pulse compression rarely, if ever, go as far as rigorously demonstrating the peak output power of the compressed pulse—typically, they simply measure FWHM pulse duration and beam focusability (M^2) separately, ignoring spatiotemporal coupling or spatial or temporal pedestal. In our experience, these two measurements are simply a starting point, and a rigorous physical measurement is necessary that is directly sensitive to peak intensity—for example, HHG in a geometry with a well-characterized near-Gaussian focus with a well-characterized target density. Anecdotally, based on our experimental experience, the typical result from a single stage of nonlinear pulse compression is a 50–80% pulse energy throughput and a ~5–6× reduction in FWHM pulse duration—but only a 1.5–2.5× increase in peak focused intensity; i.e., the "useful" pulse energy after compression can easily be 2–3× less than is measured with a power meter. However, the excess energy, though not useful for HHG, does contribute to thermal loading of the beamline elements.

The third approach, coherent beam combination combined with pulse compression, results in a relatively complex system and also is limited by the fact that pulse compression techniques suffer from rapid increase in physical size and degradation in compressed pulse characteristics for pulse energies >~1 mJ—the level we find necessary to approach optimum flux at 13.5 nm.

Nevertheless, such an approach has been successful in generating light at 13.5 nm,[52] as shown in Fig. 21.9. Reference 52 reports an overall flux from laser output to 13.5-nm light of up to 5×10^9 ph/sec/eV, which is ~4× lower in flux and means an efficiency from laser output to 13.5 nm that is ~30× lower than the aforementioned Ti:sapphire laser results. This illustrates the importance of taking a systems point-of-view for these sources: conversion efficiency in the final HHG step can vary considerably, depending on wavelength pulse duration, energy, and pulse quality. These factors can easily outweigh advantages in overall power and efficiency of the laser driving the process.

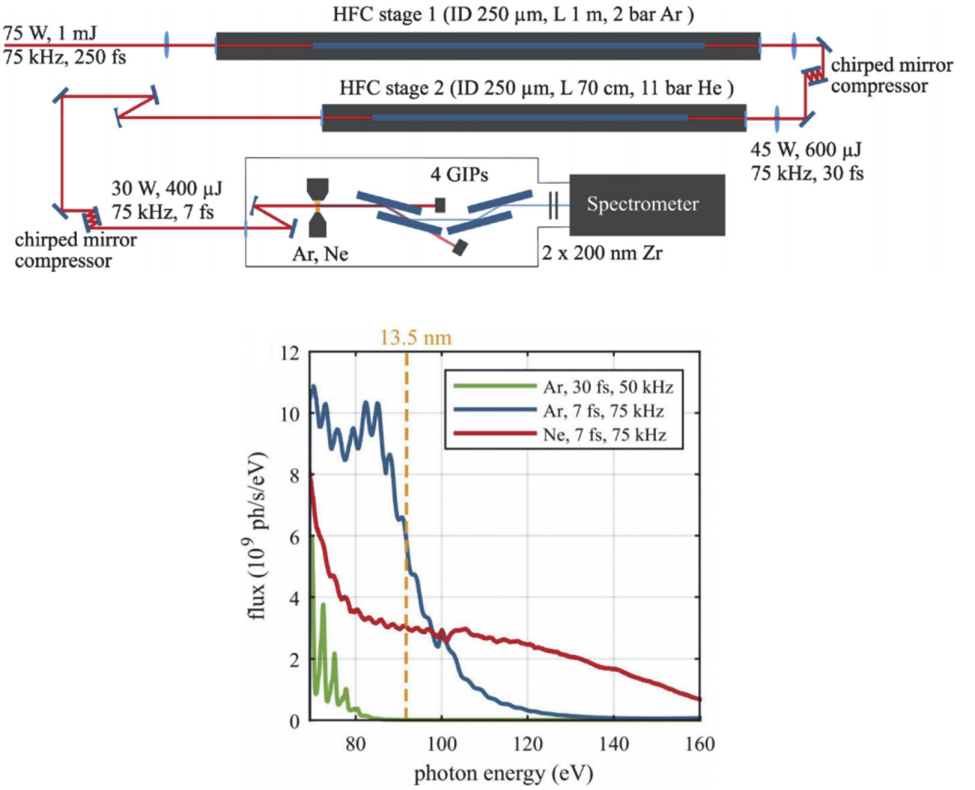

Figure 21.9 (top) Setup for generation of 13.5-nm light using a coherently combined ultrafast Yb:fiber laser, followed by two stages of pulse compression to 7-fs duration. (bottom) Graph showing the resulting flux as a function of photon energy. (Reprinted from Ref. 52).

Parametric amplifiers [which operate using optical parametric chirped-pulse amplification (OPCPA)] can also be pumped by Yb lasers,[53,54] making use of picosecond-duration pulses to generate femtosecond-duration output pulses that are broadly tunable. However, parametric amplification is a downconversion process and therefore has primarily been of interest for driving HHG with mid-infrared light, which is useful for generating high-energy HHG in the 1- to 4-nm range.[32] For light in the ~0.7- to 1-µm spectral region, which is optimum for 13.5-nm generation, OPCPA lasers are a relatively inefficient approach and furthermore are very challenging to optimize for beam quality.

In conclusion, Yb-laser-based HHG sources are practical for use at longer wavelengths but are still relatively experimental for $\lambda = 13.5$-nm generation, requiring coherent beam combination followed by multiple stages of pulse compression. Advances in the lasers, as well as new techniques for pulse compression at higher pulse energies,[55] may change this in future. However,

increased efficiency of conversion requires high-quality pulse compression at higher pulse energies than is currently routine. High-energy pulse compression work has a long history[55–57] of slow progress, the incremental pace resulting from the fact that the nonlinearities employed are difficult to control and not in any way self-limiting. Since most published results do not fully characterize peak focusable intensity and spatio-temporal distortions, the effect of these distortions on HHG efficiency inherently has a high degree of uncertainty.

21.4 Nanotechnology Applications

Coherent EUV high harmonics have demonstrated the ability to play an important role in support of nanotechnology and quantum science. EUV light has an intrinsic ability to monitor function, and the femtosecond pulse nature of the HHG source makes it possible to freeze even the fastest dynamics. The excellent spatial coherence also makes these sources ideally suited for a range of new coherent diffraction dynamics and imaging modalities.

In terms of industrial applications of high-harmonic sources, production of integrated circuits (ICs) is a large-scale nanotechnology enterprise, and the inherent resolution and sensitivity associated with short-wavelength light has potential application, for example, in detecting defects in bare wafers or patterned surfaces. Furthermore, the recent introduction of EUV lithography using 13.5-nm light into IC manufacturing creates potential opportunities, for example, for through-pellicle nanoimaging of the masks to review specific areas and to monitor mask condition in production.

21.4.1 Coherent diffractive imaging with 13.5-nm light

Coherent diffractive imaging (CDI) is an emerging collection of techniques that enable high-resolution, phase-sensitive imaging even without imaging optics. Instead of an imaging optic, CDI techniques generally allow the light to propagate freely to the detector after scattering from the sample. As a result, the field at the detector resembles the Fourier transform of the light leaving the sample, as shown in Fig. 21.10. By iteratively enforcing knowledge in the sample space and detector space, these techniques can enable phase-sensitive imaging with diffraction-limited resolution.[58] This eliminates the severe constraints imposed by conventional image-forming optics (typically, zone-plate lenses) that have previously limited resolution to $\sim > 5\,\lambda$.

While simple implementations of CDI can work well, they are often sensitive to noise and imperfect knowledge of the experiment. A CDI technique known as ptychography is able to overcome these limitations to some degree and is rapidly gaining popularity.[59] In this scheme, a coherent beam is focused successively onto several overlapping regions of the sample, and at each region, a diffraction pattern is recorded. This overlap provides inherent redundancy in the collected dataset and offers improved reliability in

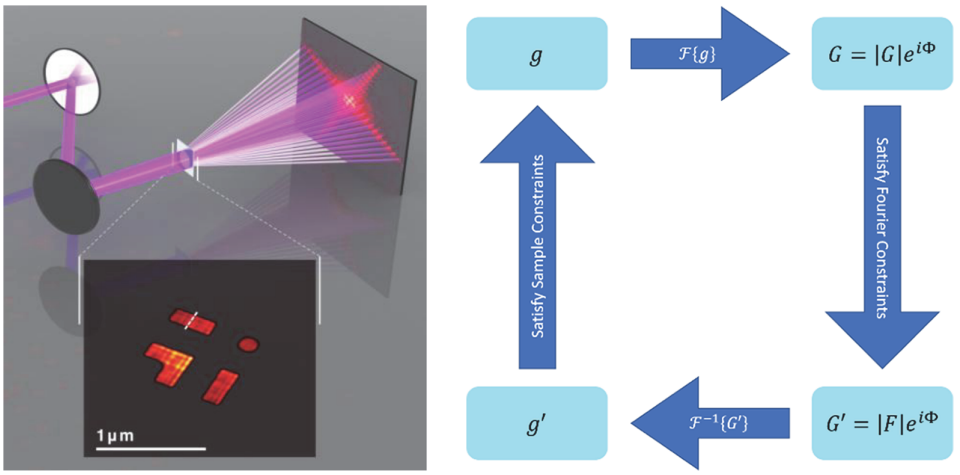

Figure 21.10 Schematic of coherent diffractive imaging. (left) Coherent light is loosely focused onto a sample, and the intensity of the scattered light is detected in the far field. Iterative phase retrieval enables high-resolution reconstruction of the complex field leaving the sample, as shown in the inset. (right) A phase retrieval algorithm enables the reconstruction of the complex field leaving the sample g by iteratively enforcing constraints on an initial guess for the sample image, which is then translated to the detector space through Fourier propagation. In the detector space, the measured amplitude of the propagated field $|F|$ can replace the computed amplitude. Repeated iterations then converge on the amplitude and phase of the exit field. (Left figure adapted from Ref. 63.)

the presence of noise or other experiment imperfections and miscalibration.[60] Furthermore, ptychography enables the robust, artifact-free decoupling of the object and the illumination, which is crucial for quantitative determination of the sample's phase shift and composition.

Coherent diffractive imaging with EUV light has exquisite chemical and elemental contrast, and its short wavelength enables few-nanometer imaging within the diffraction limit.[61,62] In particular, 13.5-nm light has been selected both for material-sensitive, high-resolution purposes and for use in EUV lithography. For this reason, several tabletop-scale and facility-scale sources are developing instruments utilizing 13.5-nm CDI.[63–67] Figure 21.11 shows example data from ptychographic CDI of a nanostructure using 13.5-nm light.[68] This work demonstrates the power of CDI over previous conventional imaging techniques, in that the demonstrated, subwavelength and NA-limited, 12.6-nm resolution is several times better than any conventional imaging implemented at this wavelength.

Ptychographic CDI can be done either in transmission or reflection geometries,[61,68–70] with the latter being uniquely suited to imaging of solid surfaces since reflection coefficients are still high in the EUV range compared with the soft-x-ray range. Imaging, for example, of buried layers in reflection is a unique capability of reflective EUV microscopy.[71]

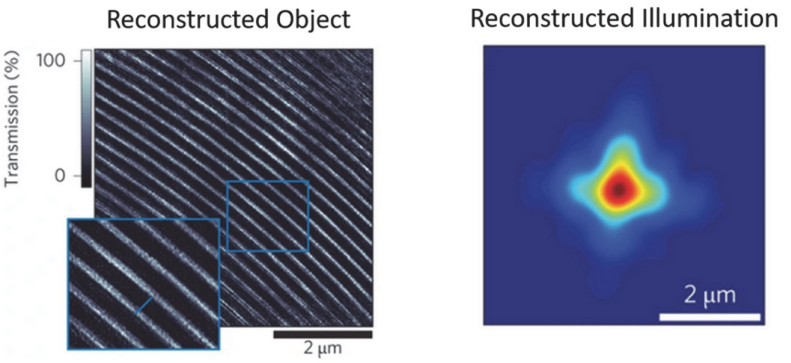

Figure 21.11 Example use of HHG as a source for new technological capabilities. (left) Coherent diffractive imaging can be used to image at the nanometer scale with unprecedented, subwavelength, 12-nm resolution. (right) The exceptionally small ~1-μm size of the refocused illumination illustrates the high spatial coherence of the source. (Reprinted from Ref. 68 © Nature Publishing Group.)

21.4.2 Imaging reflectometry for compositional analysis

EUV light is exquisitely sensitive to elemental composition, as atomic transition edges of many elements exist in or close to this wavelength range. Therefore, the complex reflectance encoded in a CDI image can be used to extract the elemental composition of regions of the object within the field of view. The fact that CDI retrieves the complex reflectance makes this application of CDI particularly interesting, since the phase shift is often more sensitive to composition than to absolute reflectance (but this information is lost or not quantitatively correct in most other imaging techniques). Moreover, a good balance of long penetration depth and high reflectance in this wavelength range means that imaging can be conducted in reflection mode, which places less severe constraints on the sample geometry and at the same time still allows probing buried interfaces and structures.

However, it is difficult to extract quantitative compositional information from a single CDI image; each pixel in an image is represented by a single complex reflectance value, which is not nearly enough information if multiple parameters about the sample are to be extracted, such as thickness of layers (if the sample has a multilayered structure) and their refractive indices, which are in turn parametrized by elemental composition and density.

To obtain enough information to solve for the parametrized model of the sample, multiple images are necessary; this will provide multiple complex reflectance values for each point within the image, which can then be used to constrain the sample model and solve for the composition. Multiple images can be taken at different wavelengths and polarizations of the incident illumination, which allows spectroscopic and ellipsometric analysis, or they can be taken at multiple incidence angles, which allows for reflectometry akin

to the ubiquitous x-ray reflectometry (XRR). This last approach is the idea behind coherent diffractive imaging reflectometry, which was first demonstrated in Ref. 72 using 30-nm EUV light generated by a HHG setup.

In this work, a test lithographic sample was imaged at five different incidence angles with ptychographic CDI. The images were then segmented into different regions, and the average difference in the phase shift upon reflection between the regions were calculated. This yielded a phase-step curve as a function of incident angle between different regions of the sample. Then, an optimization algorithm routinely used in similar reflectometry techniques was used to find a model of the sample with a theoretical phase-step curve that best agrees with the experimental curve. In this demonstration, various types of parameters in the sample model were solved for, including layer thicknesses, structure heights, interface quality, dopant levels, and experimental calibration parameters. Figure 21.12 shows the result rendered into a three-dimensional (3D) model. Uncertainty analysis revealed that this technique had a similar or higher level of precision compared to other techniques that might be used to solve for the parameters; for example, certain layer thicknesses and structure heights were solved with uncertainty on the order of angstroms.

EUV imaging reflectometry occupies a unique space in the matrix of various imaging and metrology techniques. The technique is nondestructive,

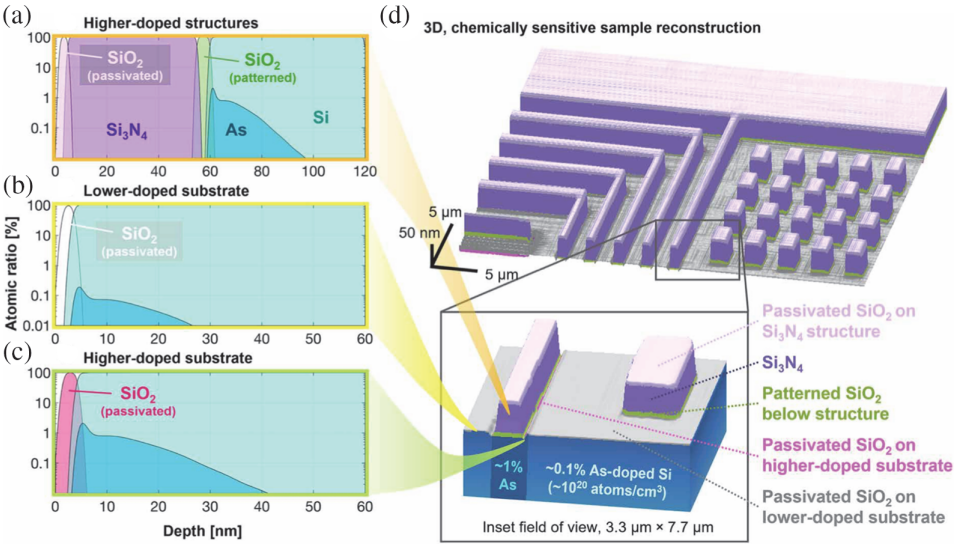

Figure 21.12 Demonstration of EUV imaging reflectometry. A test lithographic sample is imaged at multiple incidence angles using CDI, and the complex reflectance as a function of angle is used to solve for a parametrized, depth-resolved chemical composition for the various regions shown in (a)–(c). The models can be combined with the images to finally form a spatially and depth-resolved model, as shown in (d). (Reprinted from Ref. 72.)

unlike other milling (e.g., secondary ion mass spectroscopy and Auger electron spectroscopy) and cross-sectional (e.g., tomography, transmission electron microscopy) techniques. Yet imaging reflectometry is also spatially resolved, which is often not the case for other nondestructive, model-based metrology techniques (e.g., x-ray reflectometry, ellipsometry). Such techniques often require a large transversely uniform region, which means that they cannot be performed on fine structures, and are also susceptible to the presence of contamination that can corrupt the data. In contrast, imaging reflectometry provides the user the ability to choose from the imaged field-of-view regions to analyze, meaning that small structures can be analyzed, and any contamination can be excluded from the analysis. Using EUV light and CDI, the technique is able to have spatial resolution on the order of tens of nanometers but also have large fields of view of tens of microns.

The high versatility and sensitivity of this technique makes it suitable for measuring a wide variety of complex structures that can be fabricated using lithography. It is a rare technique that allows simultaneous measurement of a very wide range of parameters (composition, density, topography) in a small, localized region nondestructively. This technique requires coherent EUV light that is stable in power and pointing over a long period of time to collect multiple imaging datasets, and that this has been successfully implemented using a tabletop HHG setup is yet another indication that these light sources are capable of contributing to the development of EUV lithography and the nanotechnology systems produced by it.

21.4.3 Heat transport on the nanoscale studied with HHG light

Recently, HHG sources have also been used to probe energy flow in complex nanostructured devices—including, but not limited to, accessing thermal transport away from nanoscale heat sources. Material systems with characteristic dimensions on the nanometer scale often behave far differently than bulk materials, typically due to the increased influence of boundaries. Therefore, predicting material properties of nanoscale devices is challenging because traditional metrology tools struggle to precisely measure transport in complex systems, and conventional macroscopic models of the bulk physics fail to accurately describe the observed phenomena.

Heat transport in nanoscale geometries is no exception. In particular, semiconductor and dielectric materials display heat flow predominantly determined by the behavior of phonons, or quantized quasiparticles of vibrational energy, which can have mean free paths (MFPs) ranging from a few nanometers to hundreds of microns at room temperature.[73] The conventional model of thermal transport—Fourier's law of heat diffusion—assumes that there are sufficient phonon–phonon scattering events to establish a local thermal equilibrium (and thus define a temperature) at every point within a system. When the length scales relevant to the thermal transport are

on a similar scale as the phonon MFPs in a material, this assumption breaks down and the macroscale heat transport model fails to describe the physical behavior.[74] In some cases, when physical dimensions of the system approach that of the phonon MFPs, additional scattering from surfaces and interfaces can alter the phonon characteristics, resulting in measured thermal conduction values dependent on geometry that are considerably lower than the bulk value.[75–77] In other cases, the introduction of heat via a nanoscale source can initiate non-equilibrium behavior, where diffusion as a mechanism cannot predict the transport. This latter situation can arise even in bulk materials if the relevant transport distances considered are on the same order as the phonon MFPs. Moreover, experiments employing either structured optical excitations[78–80] or laser-heated nanostructures[81–83] have observed nondiffusive thermal transport dependent on the heat source geometry. As a result, a unified and fundamental approach to understanding thermal transport is still elusive, precluding the development of advanced nanodevices that efficiently manage heat.[84] More interestingly, these findings also indicate that nanostructuring may be used to engineer heat flow, paving the way for more efficient thermoelectrics[85] and other devices.[86]

Better measurements of the transport properties in nanoscale devices are required to validate novel models of heat flow for general situations. EUV beams via HHG sources have been utilized by several recent experiments to explore thermal transport away from nanoscale heat sources in a variety of materials.[83,87–89] By leveraging the short wavelength, spatial coherence, and ultrashort pulse duration of these sources, experiments can more precisely access the phonon behavior at smaller length- and timescales than traditional techniques based on visible lasers. The short wavelength and spatial coherence allow HHG-based techniques to probe the transient heat flow from periodic hot spots with tens of nanometer sizes and spacings;[87,88] whereas, visible-based methods are often diffraction limited to probing micron lengthscales.[78,79] However, by fabricating complex nanostructured transducers on sample surfaces, visible lasers have measured the thermal transport from 30-nm-wide heat sources on the surfaces of specific materials.[81] Unfortunately, these experiments typically need to remove the first 100 or more picoseconds of the signal because visible wavelengths are highly sensitive to hot electrons, which mask the thermal transport. On the other hand, EUV-based techniques can selectively probe the phonon behavior on ultrafast and longer timescales by tuning the wavelength from absorption edges.[90,91]

EUV beams via HHG have been implemented in a pump–probe scatterometry experiment to probe thermal transport at the nanoscale. Typically, periodic arrays of metallic nanostructures—with sizes as small as 15 nm and periods as small as 45 nm—are fabricated on the surface of the sample. A visible-to-infrared femtosecond laser pulse is used to impulsively excite the metallic nanostructures, known as the pump pulse. The coherent

excitation of the structures launches acoustics waves—which will be discussed in the following section—and the heated structures dissipate their thermal energy into the sample. An EUV probe pulse generated via HHG is incident on the sample at a controlled time delay after the pump pulse, diffracts from the sample's nanostructured surface, and is collected onto an EUV-sensitive CCD. The surface deformation is then observed with picometer sensitivity by monitoring the change in diffraction efficiency of the EUV light. This surface deformation is directly related to the acoustic and thermal dynamics occurring in the sample and nanostructures. A schematic of this setup is shown in Fig. 21.13. Both the optical pump and EUV probe beam are derived from the same laser, giving the system inherent timing stability. Therefore, snapshots of the evolving physics on the surface can be captured with femtosecond resolution. A notable advantage of HHG sources is that the conditioning of the beam can be performed using traditional optical components before the driving laser is upconverted to EUV. This negates the need for complex manipulation of the EUV beam under vacuum in a wavelength regime where optics are scarce, which is typically required for facility scale sources.

For exotic samples, the fabrication of nanostructures on the surface may not be feasible without damage to the material of interest. In this case, the nanostructures can be substituted for the interference of two coherent lasers pulses in the sample to create a sinusoidal excitation in a transient grating (TG) technique.[92] Probing the dynamics launched by an optical TG excitation

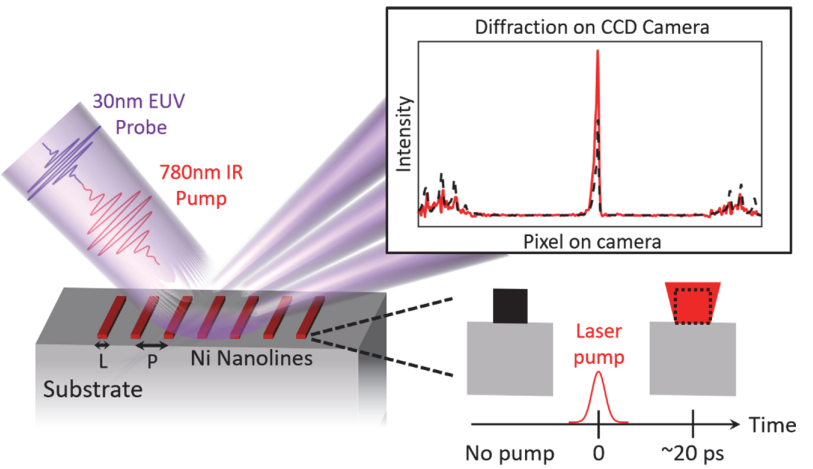

Figure 21.13 Schematic of the typical dynamic EUV scatterometry experimental setup. Ultrafast pump pulse in the infrared (IR) range illuminates periodic arrays of metallic nanostructured transducers on a sample surface. The IR light is preferentially absorbed by the nanostructures, causing rapid heating. The accompanying impulsive thermal expansion launches both acoustic and thermal dynamics. An EUV probe pulse via a HHG source incident on the sample surface is diffracted onto a CCD camera. Displacements in the sample surface alter the diffraction efficiency, allowing for picometer sensitivity to the launched dynamics. (Reprinted from Ref. 88.)

with a HHG source has already been demonstrated;[93] however, in practice, this technique is diffraction limited by the visible wavelengths to excitation periods of ~500 nm, in similarity to its fully optical counterpart. To launch nanometer-scale dynamics, a TG setup with two crossed, coherent EUV or soft-x-ray pulses is required. Recent work from high-pulse-energy x-ray free-electron lasers has demonstrated excitation with EUV interference patterns,[94,95] but work to apply this pump–probe technique to HHG sources is ongoing (see Section 21.4.5 for more discussion).

This dynamic EUV scatterometry technique, with an excitation generated via laser-heated nanostructures, has uncovered novel and unexpected thermal transport regimes,[83,87,88] mapped the geometry dependencies on the heat flow,[88,89] and even validated new microscopic and mesoscopic models of phonon behavior.[89,96] Using HHG sources, Siemens et al. first observed that Fourier's law drastically underpredicts the thermal dissipation efficiency as the size of a heat source on a bulk substrate becomes comparable to the dominant phonon MFPs in that material.[83] Recently, in a similar experiment, Hoogeboom-Pot et al. found that not only the size, but also the spacing, of heat sources changes the rate of thermal dissipation when compared with simple bulk models.[87] Specifically, the authors showed a surprising behavior of thermal transport, where closely spaced nanoscale heat sources cool faster than widely spaced, as shown in Fig. 21.14. Frazer et al. quantitatively

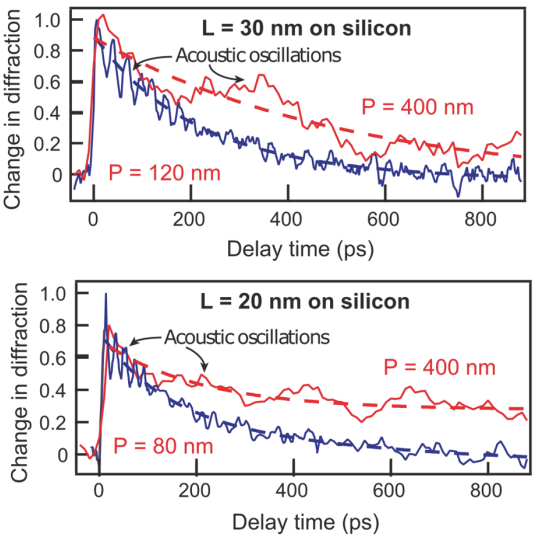

Figure 21.14 Dynamic EUV scatterometry change in diffraction signal for varying-size and varying-spacing periodic arrays of nanostructured heat sources on silicon. The top (bottom) panel compares heat sources of size $L = 20$ nm (30 nm) with different periods P. The oscillations in the data arise from acoustic waves launched by the coherent excitation of the periodic nanostructures, while the decay of the signal (dashed lines) follows the cooling of these heat sources. Surprisingly, the closely spaced nanoscale heat sources (blue) cool faster than widely spaced ones (red). (Reprinted from Ref. 87.)

mapped the deviations from Fourier's law as a function of both the size and spacing of nanoscale heat sources, validating the counterintuitive predictions of Hoogeboom-Pot et al.[88] In these studies, the nondiffusive heat flow was quantified by fitting an effective thermal boundary resistivity between the nanostructure and the substrate to show that the resistivity deviates from the intrinsic value, as displayed in Fig. 21.15.

In Fig. 21.16, the results of this quantification as a function of size and spacing from Frazer et al.[88] is shown. As the size of the heat sources becomes comparable to the phonon MFPs in the substrate, a decrease in the cooling rate of the nanostructure compared to the bulk Fourier's law model is observed—signified by an increase in the effective thermal boundary resistivity (black finely dashed). However, as the spacing of the heat sources becomes comparable to the phonon MFPs, the heat transport efficiency increases (blue solid), returning towards the bulk diffusive prediction. If at this point, the spacing is increased, causing the heat sources to become increasingly isolated, the transport will again rapidly decrease in efficiency (red dashed).

Beardo et al. recently verified that these same counter-intuitive dependences on heat source geometry exist for not only for periodic nanolines but also for periodic nanodots.[89] Due to the unique information accessed by HHG sources, multiple works were able to provide new fundamental understanding to thermal transport in semiconductor and dielectric materials. Siemens et al.[83] and Hoogeboom-Pot et al.[87] proposed phenomenological models to provide intuitive explanations to the observed behavior.

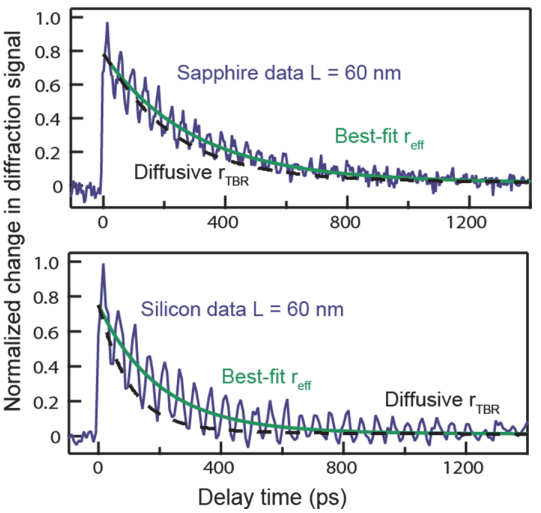

Figure 21.15 Change in diffraction efficiency signal (blue curves) from the dynamic EUV scatterometry technique for 60-nm-size (L) nanostructures on both sapphire (top) and silicon (bottom) substrates. The diffusive prediction via bulk Fourier's law (r_{TBR}, where TBR is thermal boundary resistivity) is shown in black and is in clear disagreement with experimental data. The degree of nondiffusive thermal transport can be quantified by fitting an *effective* thermal boundary resistivity (r_{eff}) to the data (green curves). (Reprinted from Ref. 87.)

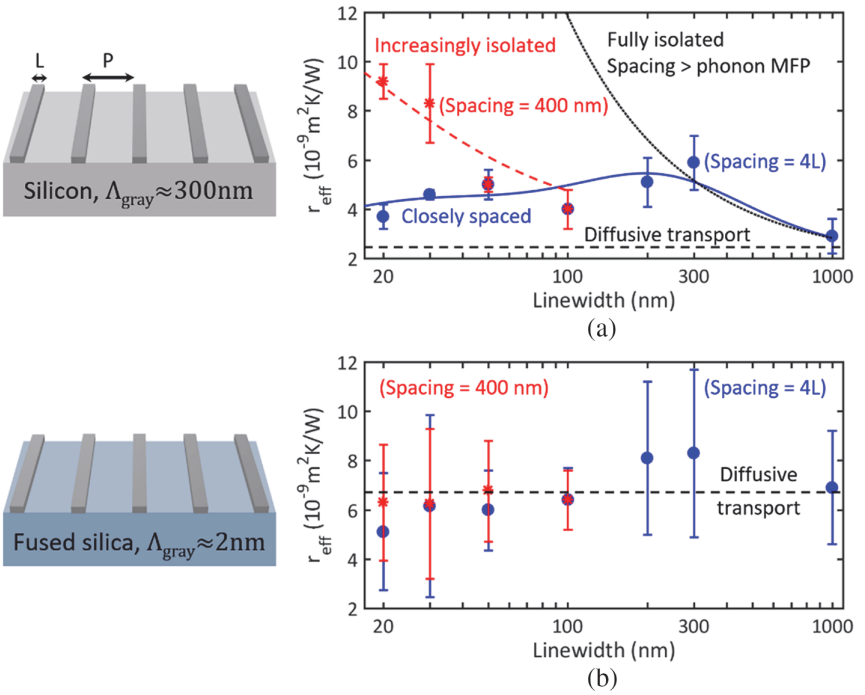

Figure 21.16 The fitted effective thermal boundary resistivity r_{eff} as a function of the nanoscale heat source size (linewidth L) and spacing P for both silicon and fused silica. (a) For large linewidths, the experimental data (blue dot at linewidth = 1000 nm) agree with the diffusive transport predictions from bulk Fourier's law. However, as the linewidth approaches the average phonon MFPs in silicon (~300 nm), the heat dissipation efficiency from the nanostructures reduces, signified by an increase in r_{eff} (fully isolated prediction, black finely dashed curve). However, as the spacing becomes comparable to the phonon MFPs, the heat dissipation efficiency increases, returning towards the diffusive transport prediction (blue dots, blue curve). Note that for the data shown in blue, the spacing of the structures is 4L. Thus, a decrease in L is accompanied by a decrease in P. If P is held constant as L is reduced, then the heat dissipation efficiency again decreases (red asterisks, red dashed curve). (b) The thermal transport does not depend on the heat source geometry because the average phonon MFPs in fused silica (~2 nm) are well below the measured sizes. (Reprinted from Ref. 88.)

Beardo et al. demonstrated that a new and general hydrodynamic transport model, validated by dynamic EUV scatterometry, accurately predicts—without the need for geometry-dependent fit parameters—the heat flow from nanoscale sources in arbitrary geometries.[89] Moreover, Honarvar et al. utilized recent results from HHG-based experiments to discover the microscopic scattering mechanisms responsible for the previously observed surprising behavior.[96] In summary, experiments utilizing EUV beams via HHG sources can access thermal transport on length- and timescales beyond traditional visible-based techniques, facilitating deeper insights into fundamental behavior critical for the development of nano- and quantum technologies.

21.4.4 Mechanical properties at the nanoscale

Heat flow is not the only material behavior accessible by HHG sources. With wavelengths and pulse durations in the nanometer and femtosecond regimes, respectively, these tabletop EUV sources are also well equipped to probe the mechanical and structure properties of ultrathin and nanostructured systems. The demand for faster, more efficient, and more compact nanoscale devices (such as chips for portable electronics) drives engineers to develop increasingly complex designs with more 3D architectures that push the limits on fabrication capabilities and available material properties. Therefore, a broad range of applications—including, but not limited to, nanoelectronics, quantum devices, solar cells, and energy materials—often relies on the precise fabrication of nanostructures and ultrathin films that can now have dimensions down to single-atomic layers. However, characterization of the mechanical and structural properties of nanostructured and layered devices to comparable precision is currently beyond the capabilities of many traditional techniques, which is a roadblock for many of these technologies, including nanoelectronics.[97]

While many traditional approaches exist to measure the elastic properties of films and nanostructures, these techniques struggle to probe devices when dimensions fall below 100 nm, or even 10 nm. Nanoindentation is a potentially destructive, versatile technique that can easily characterize the mechanical properties of thin films. However, accessing the properties of submicron-thick layers quickly becomes challenging and requires complex modeling as sizes approach 100 nm.[99,100] Techniques based on visible lasers—such as Brillion light scattering[101] or picosecond ultrasonics[102]—can successfully characterize the elastic properties of thin films. However, the diffraction limit of the probe light often makes the properties of $<$100-nm films inaccessible. Nonetheless, impressive advances in modeling and experimentation have pushed these techniques beyond this limit for specific material systems.[103–105] Still, experimental elastic and structural characterization of films, nanostructures, and complex materials in general geometries with dimensions below 10 nm remains an outstanding challenge.

HHG sources incorporated into an *identical* pump–probe scatterometry setup as described in Section 21.4.3 can launch and observe nanoscale acoustic waves that probe near-surface mechanical properties. As illustrated in Fig. 21.17, an ultrafast, infrared pump laser induces rapid heating primarily in periodic arrays of metallic structures patterned on the surface of a thin film or sample of interest. The resulting impulsive thermal expansion of the structures excites a variety of acoustic modes that propagate through the substrate, film, and nanostructure. On shorter timescales, typically picoseconds, longitudinal acoustic waves (LAWs) traveling in the cross-plane direction reflect off of interfaces and surfaces. A LAW trapped in the metallic structure creates resonant ‘breathing modes’ with frequencies related to the

patterned grating's properties. A LAW traveling in the thin film will reflect from the film–substrate interface, returning to the surface in an echo carrying information regarding the film's mechanical properties and thickness. On longer timescales (typically picoseconds to nanoseconds), the coherent excitation of the grating launches surface acoustic waves (SAWs) with wavelengths λ_{SAW} set by the grating period. SAWs are uniquely confined to the sample surface penetrating a depth δ_{SAW} proportional to their wavelength: $\delta_{SAW} \sim \lambda_{SAW}/\pi$.[98,106] Therefore, long-wavelength SAWs propagate predominantly in the substrate, while sufficiently short-wavelength SAWs can be confined to the thin film.

The surface deformation resulting from the LAWs and SAWs can be exquisitely monitored with picometer sensitivity by diffracting an EUV pulse off the grating at a precisely controlled delay time.[90,98] As shown in Fig. 21.17, the calculated experiment signal contains the frequency of the SAWs, the thin-film LAW echoes, and the resonant nanostructure LAW. As HHG sources emit coherent light with nanometer wavelengths, these EUV sources can diffract from, and therefore detect, SAWs with nanometer-scale

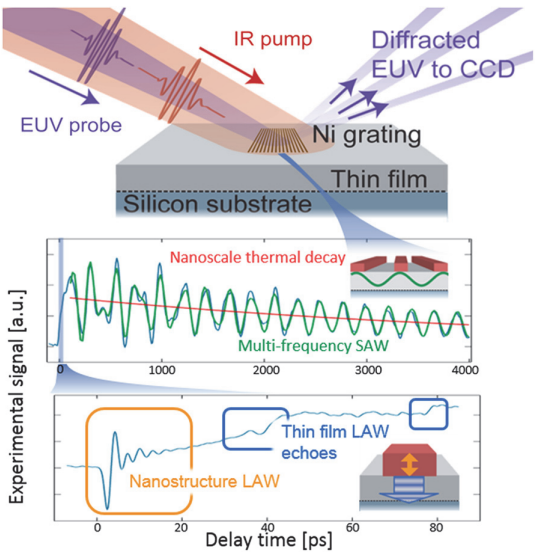

Figure 21.17 Pump–probe EUV scatterometry using HHG sources accesses thermal transport and acoustic wave propagation in a single measurement. (top) An infrared (IR) pump pulse excites thermomechanical behavior in the Ni grating, thin film, and substrate that is observed by a diffracting coherent EUV probe pulse collected on a detector. (bottom) The experimental EUV diffraction signal is plotted as a function of delay time between the pump and probe pulses. On shorter timescales (lower plot), a LAW trapped in the metallic grating creates resonant breathing modes (orange), while a LAW traveling in the film echoes from the film–substrate interface (blue). On longer timescales (upper plot), the coherent excitation of the grating launches SAWs with periods set by the nanostructure periodicity (green). (Reprinted from Ref. 98.)

wavelengths in the hypersonic frequency range. These SAWs are confined to the near-surface, and at sufficiently small wavelengths, their speed is a function of only the thin-film properties, independent of the substrate. The SAW frequency and LAW echo times can then be related to the thin film's elastic tensor, allowing for the full characterization of films only nanometers in thickness.[98]

Multiple works have already demonstrated the versatility of pump–probe EUV scatterometry based on HHG sources: for example, this technique can characterize the full elastic tensor of ultrathin films <5 nm in thickness,[107] possesses monolayer sensitivity to nanostructured layers,[108] and probes the mechanical and structural properties of nanostructured metamaterials.[109] Siemens et al. provided an initial demonstration of EUV scatterometry by extending optical measurements of SAWs launched by laser-excited gratings to the EUV.[110] The authors used a HHG source to map the SAW dispersion in the presence of periodic structures. Nardi et al. then developed theoretical models of the thermomechanical behavior in EUV scatterometry experiments.[111] Li et al. extended these measurements to demonstrate generation and control of SAWs down to 45-nm wavelengths, which corresponds to $\delta_{SAW} \sim 10$ nm.[112] Based on these works, pump–probe EUV scatterometry could then be extended to extract the mechanical properties of nanostructured and complex materials. Hoogeboom-Pot et al. measured the elastic properties of nanostructured Ni/Ta bilayers.[108] By carefully observing frequency shifts in the propagating SAW and resonant LAW modes, the authors extracted the density ratio and acoustic wave speed in layers down to 1 nm in thickness, finding deviations from bulk properties likely due to the nanoscale dimensions. Hernandez-Charpak et al. and Frazer et al. characterized the full elastic tensor of a-SiC:H and a-SiCO:H ultrathin films for applications as low-dielectric constant interlayers to improve the efficiency and speed of nanoelectronics.[98,107] These works found that both doping and thickness can drastically alter the mechanical properties of ultrathin films. Hernandez-Charpak et al. corroborated measurements observing a decrease in Young's modulus of the film as hydrogen doping is increased and uncovered a previously unobserved transition from brittle to ductile behavior in these films once the hydrogen doping sufficiently disrupts the bond network connectivity.[98] In similar films, Frazer et al. observed nearly an order-of-magnitude decrease in Young's modulus as the thickness decreased by nearly an order-of-magnitude.[107] The authors interpreted their results in terms of the coordination of bulk versus surface atoms to understand the interplay of doping and structure on the mechanical properties, as shown in Fig. 21.18. Moreover, they demonstrated that EUV scatterometry can extract the full elastic tensor of a <5-nm single film within a bilayer. More recently, Abad et al. extended these measurements from uniform single layers to probe the properties of complex metamaterials.[109] The team used HHG sources to

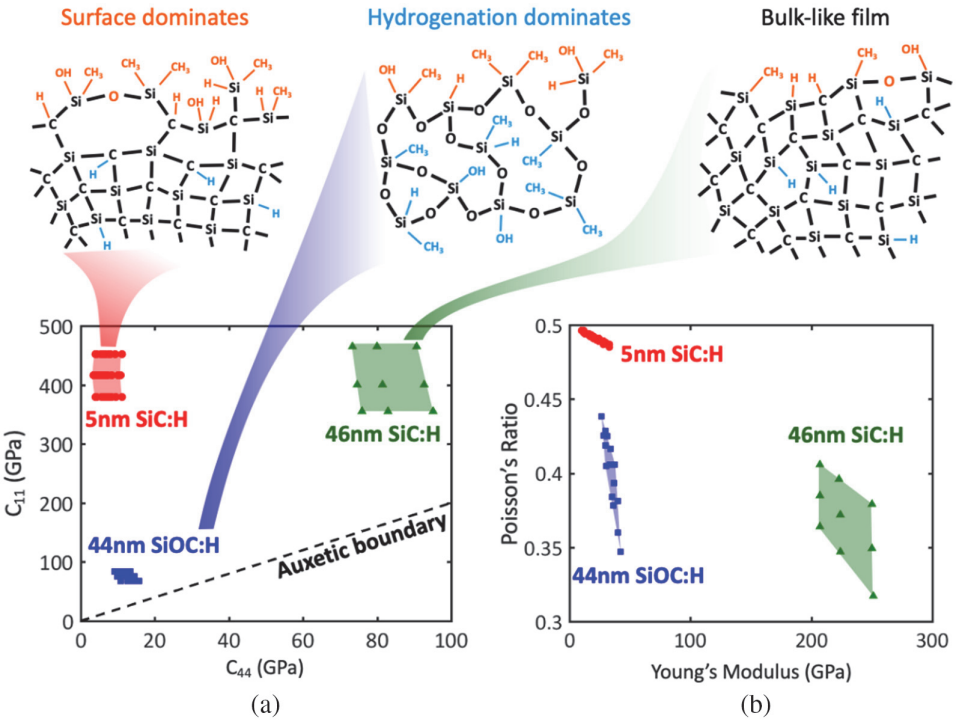

Figure 21.18 Influence of surfaces and dopants on the elastic properties in dielectric a-SiC:H and a-SiCO:H ultrathin films. (a) The two components of the elastic tensor extracted for films of different composition, thickness, and doping. (b) Identical data as in (a) except converted to Young's modulus and Poisson's ratio. The data points and shading represent the error in the measurement. (green) 46-nm-thick a-SiC:H film with low hydrogen doping (hydrogenation) displays the expected bulk-like elastic properties. (blue) 44-nm-thick SiOC:H film with high hydrogenation is much more compliant (i.e., a much lower Young's modulus) because the bond network has been disrupted by the hydrogen doping. (red) 5-nm a-SiC:H film with low hydrogenation, identical to the other a-SiC:H film shown in green, and also displaying much more compliant behavior owing to the higher proportion of terminated bonds at the surface, a distinct effect from the softening due to doping. (Reprinted from Ref. 107.)

measure the acoustic dispersion, Young's modulus, and thickness, and even to verify the filling fraction of silicon metalattices—nanoscale colloidal crystals of silica spheres with the interstitial space infiltrated with polycrystalline silicon. By observing the acoustic wave dispersion for long-wavelength SAWs (~1000 nm), the authors nondestructively extracted the thickness for these complex 3D metamaterials, comparing results to cross-sectional SEM; and, by probing short-wavelength acoustic waves (~100 nm), they measured Young's modulus, comparing to theoretical calculations and nanoindentation, as shown in Fig. 21.19.

The pump–probe EUV scatterometry experiment described in Figs. 21.13 and 21.17 is limited to measuring the thermal and acoustic dynamics launched

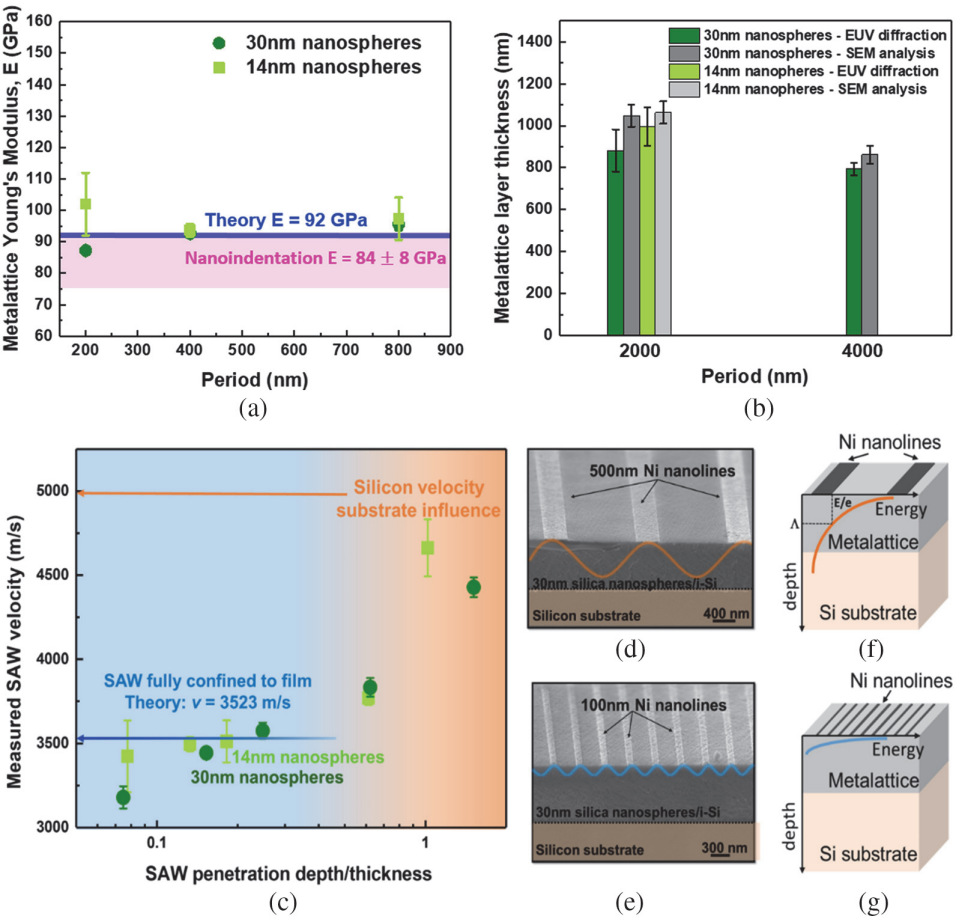

Figure 21.19 EUV scatterometry nondestructively measures the structural and mechanical properties of complex metamaterials. (a) The observed SAW velocity as a function of penetration depth, which is set by the grating periodicity, normalized to the sample thickness. Measurements on two different metalattice samples are shown: 30-nm-diameter (circles) and 14-nm-diameter (squares) silica nanosphere templates infiltrated with polycrystalline silicon. (b) and (d) Large-period gratings launch long-wavelength SAWs that penetrate the substrate, resulting in a velocity between that of silicon and the metalattice. (c) and (e) Small-period gratings launch short-wavelength SAWs that are confined to the metalattice, resulting in a velocity near the theoretical value for the metalattice. (f) Extracted values for the metalattice Young's modulus as a function of the measured grating periodicity, validated by nanoindentation and theoretical calculations. (g) Extracted values for the metalattice thickness as a function of the measured grating periodicity, validated by cross-sectional electron microscope analysis. (Adapted from Ref. 109.)

by periodic metallic structures. However, by combining this technique with the lenless imaging methods described in Section 12.4.1, Karl et al. demonstrated a pump–probe imaging capability based on HHG sources.[69] The authors captured a stroboscopic movie of the thermal and acoustic

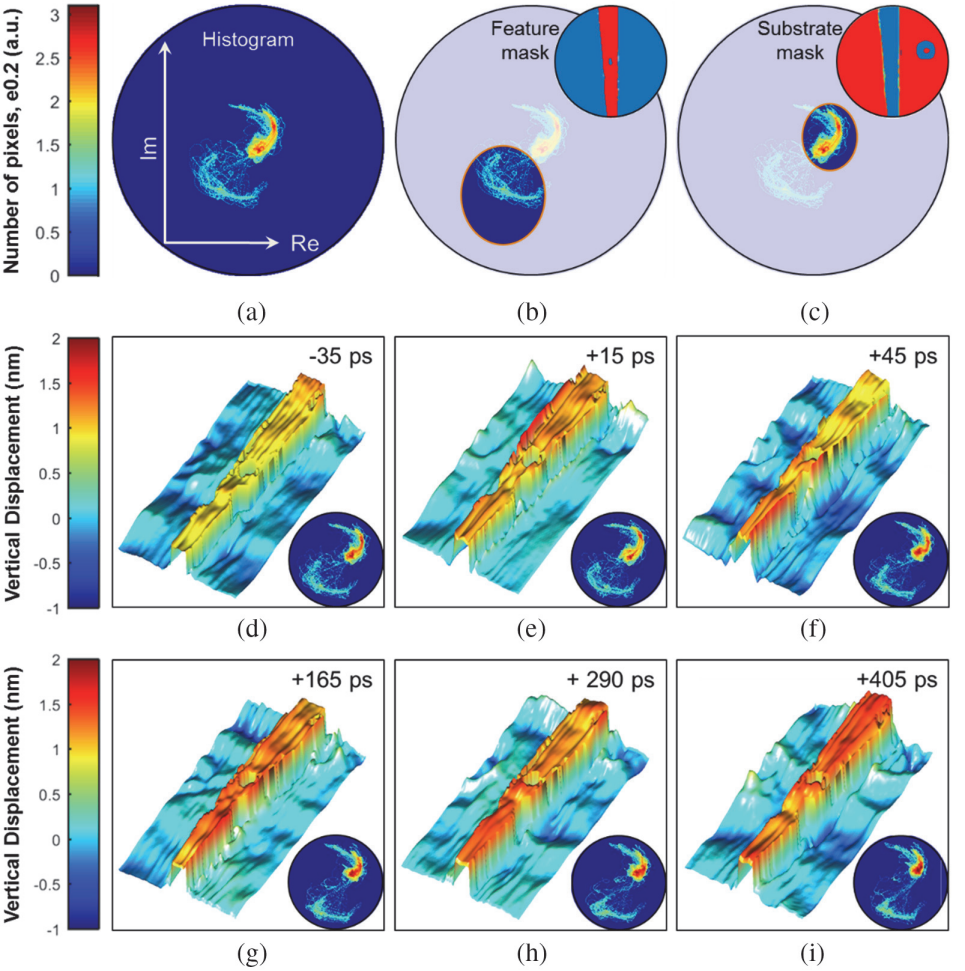

Figure 21.20 Pump–probe imaging of thermal and acoustic behavior in a nanostructure using EUV light from a HHG source. (a) A histogram of the complex reflectance values for a static image of a Ni tapered nanoantenna on a silicon substrate. (b) (c) Masking in the histogram allows one to segment the structure from the substrate in the image. (d)–(i) The reconstructed vertical surface displacements at different time delays (negative times represent moments before the structure is laser heated). The shown area is $\sim 7\ \mu m \times 12\ \mu m$. (Reprinted from Ref. 69.)

response of a laser-excited isolated nanoscale antenna with $<$100-nm transverse and 0.5-Å axial spatial resolution and with $\approx$10-fs temporal resolution (Fig. 21.20). Moreover, the team extracted the dispersion of the lowest-order SAW launched by a nanoscale antenna. These advancements in pump–probe EUV scatterometry and imaging demonstrate that HHG sources are critical tools for illuminating properties and behavior in complex nanostructured devices.

21.4.5 Interference lithography for resist characterization

The prime motivation for the semiconductor industry's shift to EUV lithography (EUVL) is to continue Moore's law in increasing the density and speed of nanoelectronics. EUVL will allow smaller feature sizes to be printed while increasing yield and productivity by providing enhanced resolution in fewer steps.[113,114] The new wavelength and small features introduce a host of new challenges. Environmental challenges include operating in vacuum with strict thermal and vibrational stability requirements. However, one of the most difficult challenges lies in developing *and testing* EUV photoresists to give optimal performance with 13.5-nm light.[115–117] During most of its development, EUVL has lacked an important supporting technology: a viable *coherent* laser-like 13.5-nm EUV source to allow for interference lithography, that can be used to test the resolution limits of resists well in advance of the development of direct printing capabilities. This gap in capability can now take advantage of both the accessibility and inherently high coherence of EUV light produced via tabletop HHG sources.

Interference lithography (IL) is the process of printing regular patterns on a sample by interfering two coherent light sources at the sample surface in a photoresist. Currently, the most common methods of performing IL with EUV light involve either split-and-recombine schemes or the use of diffraction gratings to create the desired interference pattern (Fig. 21.21). These simple setups allow for the production of regular arrays (e.g., lines and spaces or contact holes) without the use of complex optical systems or expensive photomasks.[118] Such a system has the advantage of having a relatively forgiving depth-of-focus requirement while also being reasonably tolerant of contamination. A simple two-beam interference setup creates a fringe pattern with the period proportional to the wavelength λ and inversely proportional to the sine of the half-crossing angle between the two beams θ, given by the relationship $\frac{\lambda}{2} / \sin(\theta)$.[118,119] These linear patterns can be useful on their own, for example, as diffraction gratings, but also as a means to test resolution limits of photoresists.[120,121]

The ultimate lithographic resolution of a photoresist is determined both by the optical parameters of the lithographic setup (i.e., illuminating wavelength and numerical aperture) and the photochemical response of the resist itself. While decades of R&D into lithographic sources and optical design have led to highly understood and (nearly) optimized lithographic EUV systems, far less is known about the subsequent photochemical transformation that occurs in a photoresist after exposure.[116] While a complete overview of the current knowledge of EUV-induced radiation chemistry in photoresists is beyond the scope of this chapter (for an excellent overview, see Ref. 122), we briefly highlight the current understanding of the radiochemical pathway that leads to formation of a printed image in a developed photoresist.

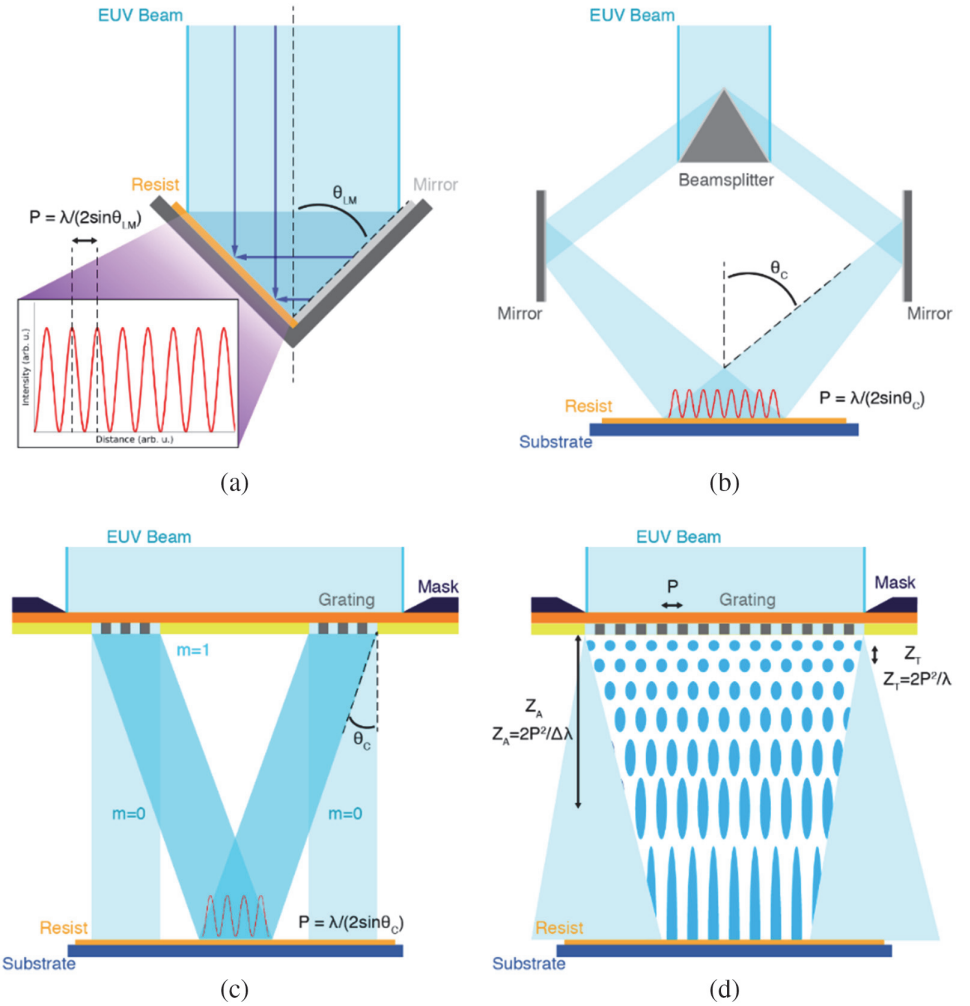

Figure 21.21 Schemes for performing IL with spatially coherent 13.5-nm EUV light. (a) Lloyd's mirror (LM) IL. Rays that are partially reflected from a mirror interfere with rays that directly impinge on the resist (dark-blue lines), creating an interference pattern (lower-left inset) with a pitch *P* determined by the relative angle of the LM (θ_{LM}) with respect to the EUV beam. (b) Split-and-recombine IL (two-beam), where the incident EUV beam is split into two beams that are then spatially overlapped at the resist plane to create an interference pattern with a pitch determined by the half-crossing angle θ_C of the two beams. (c) Transmission grating IL, where the first-order diffracted beams are spatially overlapped at the resist plane to form an interference pattern. (d) Achromatic Talbot lithography, where the Talbot effect (periodic re-imaging of a grating) is used to directly imprint an aerial interference pattern on the resist.

When an EUV photon is absorbed by a photoresist, a primary photoelectron is generated that then generates secondary electrons. The resulting wide range of electron energies (~0–70 eV) reacts with the chemical

component of the resist. In EUVL, it is the interaction of these primary and secondary electrons that drives the chemical transformation, leading to a solubility change and, after development, the final relief pattern in the resist. These photoelectrons have non-negligible MFPs compared to the critical dimensions of lithographic patterns required for current and future technology nodes, resulting in image blur and less-than-ideal printed features in the lithographic process. The situation is perhaps more severe for chemically amplified resists (CARs), as these resists contain additional molecular species (e.g., photoacids, quenchers, etc.) that have their own diffusion characteristics and local density variations that can affect resolution and line-edge roughness in the final relief pattern. Non–chemically amplified resists such as metal oxide (MOx) resists do not suffer from diffusion-induced image blur, but they are 1–2 orders of magnitude less sensitive, which increases the probability of stochastic defects for a given EUV dose.

To mitigate the electron- and photoacid-induced image blur, synthetic chemists continually tweak the chemical formulation of photoresists in an effort to improve their resolution and efficiency by suppressing unwanted chemistries during the EUV exposure process. However, regardless of the photoresist formulation, there is a complex radiochemical pathway that separates the formation of the aerial image by the lithographic system and the final relief pattern obtained after development of the photoresist, and not all of these pathways may lead to a desired result and need to be mitigated if possible. While a large research effort is now concentrated on understanding the radiochemical pathways of EUV photoresists, the rapid development of new resist formulations creates an urgent need for accessible systems that can rapidly screen new resist formulations in order to quantify their ultimate resolution and performance metrics for HVM in future technology nodes. In this sense, IL systems can provide an ideal platform for the rapid screening of photoresist for current and next-generation technology nodes.

The coherence requirement for IL helps to differentiate appropriate sources. Tin plasma–based sources are powerful but largely incoherent. Incoherent sources lend theselves well to the mask-based imaging lithography currently employed for high-throughput manufacturing; however, due to the cost and complexity of EUV scanners, they are not practical for fast-paced R&D. Commercial Z-pinch sources are similarly incoherent while producing far lower EUV flux, thus making them well-suited for inspection rather than printing purposes.[123] On the other hand, while synchrotrons and free-electron lasers (FELs) can be excellent sources of bright and coherent EUV light, they are the most expensive and inaccessible source, most often being user facilities at the national level. Alternatively, capillary discharge sources at 13.5 nm have been demonstrated,[124] but these currently offer short lifespans and low repetition rates, and are not commercially available at this time. In contrast, highly coherent and bright EUV beams can be produced by much

more-accessible and lower-cost tabletop HHG sources that are commercially available for lab use today.[125] This make HHG sources uniquely capable for use in IL and photoresist R&D.

Performing IL with a HHG source can be a powerful technique. Since, in principle, the crossing angle between the interfering beams can be continuously tuned, IL offers straightforward and precise control over the resulting interference pattern and thus the printed feature size. Additionally, the near-Gaussian-shaped intensity profile of HHG EUV beams provides a unique advantage for studying effects of dose on the critical dimensions and roughness features of a printed IL pattern. Since the intensity varies across the overlap region of the two beams, so too does the dose, which enables mapping of an entire contrast curve in a single exposure site. Moreover, the high spatial beam mode quality of bright, HHG-based EUV light enables tight focusing of the radiation, which can provide high on-target flux and rapid exposure times for many common resist formulations. Together, these features allow the performance and stochastics of particular resist formulations to be rapidly tested.

While HHG-based EUV sources have great potential for being used in IL studies, several technical challenges must be overcome in order for these sources to be used effectively. First, the lower flux of HHG-based sources (as compared to EUV scanners, synchrotrons, and FELs) demands a photon-efficient IL setup, such as the split-and-recombine or Lloyd's mirror (LM) methods shown in Figs. 21.21(a) and (b). Additionally, HHG sources inherently produce femto-to-attosecond pulses, dramatically shorter than the nanosecond pulses produced by the tin-plasma scanner sources. These short pulses are not intense enough to introduce nonlinear effects in the resist response but do place strict demands on the temporal overlap needed for forming the resulting interference pattern. As a corollary, vibrations and environmental disturbances need to be kept to a minimum to prevent blurring of the aerial image that would degrade the IL pattern. While this effect is minimized with grating-based IL schemes [Figs. 21.21(c) and (d), these methods greatly reduce the on-target photon flux and significantly increase exposure times. Finally, the HHG source itself must have high and stable flux at 13.5 nm as well as excellent pointing and beam mode quality. Thankfully, recent advances in high-flux HHG systems based on hollow-core capillaries[125] (see Section 21.3) have finally resulted in tabletop systems that possess the necessary flux, stability, and beam mode quality required for demanding IL applications at the sub-40-nm pitch level.

Despite the demanding challenges of performing IL with a HHG-based source, one particular scheme has proven successful for EUV IL using these coherent sources. In a first demonstration, Kim and coworkers utilized a LM device to print a sub-200-nm pitch pattern (e.g., lines and spaces) in a positive-tone electron-beam photoresist (ZEP520A, Zeon Specialty Materials) using coherent EUV light at 29 nm ($\partial\lambda/\lambda \cong 4\times10^{-3}$).[126] In the LM setup, a

photoresist and reflector are physically contacted at a 90-deg angle and mounted in a rotation mount. The device is placed in the EUV beam path such that the impinging EUV beam partially reflects from the reflector and interferes with the direct beam on the photoresist. This results in an interference pattern of lines-and-spaces on the photoresist with a pitch defined by $P = \lambda/(2\sin\theta)$ [as shown in Fig. 21.21(a)], with the interference angle set by the relative angle of the LM with respect to the incoming beam [Fig. 21.21(a)]. This relatively simple setup allows for straightforward tuning of the pitch pattern via the LM angle Θ_{LM} while also being robust to vibrational noise. However, the short-pulsed nature of the EUV light results in a slippage of temporal overlap moving away from the resist–reflector interface, resulting in a rapid decrease in contrast and a relatively small exposure area. Nevertheless, a pitch pattern extending over tens of microns with good contrast was achieved in this first study,[126] thus demonstrating that HHG-based EUV sources are capable of printing dense pitch patterns for EUV IL studies.

While the Kim et al.[126] study demonstrated the potential of HHG-based sources to be utilized for IL lithography at the submicron level, in order to benefit photoresist R&D, EUV IL should be performed at the actinic wavelength of EUV scanners (13.5 nm) and at pitch levels commensurate with current and future technology nodes (i.e., sub-40-nm pitch level). To this end, researchers at Imec's AttoLab have recently demonstrated sub-22-nm pitch patterning using high flux, coherent light at 13.5 nm with a LM device.[127] Despite the femtosecond pulse duration of the 13.5-nm light used in this work, the authors achieved lithographic printing of a ~20.5-nm pitch with an overall exposure field of ~1 μm in a negative-tone MOx resist (Fig. 21.22). This result is commensurate with state-of-the-art pitch patterns produced on more expensive EUV scanners and thus demonstrates that HHG-based EUV

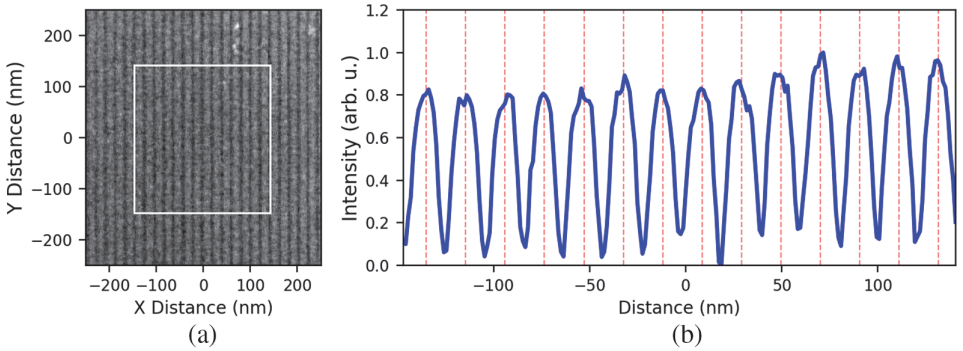

Figure 21.22 Lloyd's mirror IL with a 13.5-nm HHG-based EUV source in Imec's AttoLab (the setup of Fig. 21.7 with specifications similar to those given in Table 21.1). (a) SEM image of the interference pattern formed in a MOx resist, at a dose of ~50 mJ/cm^2. (b) Vertical integration of the SEM image intensity in the region defined by the white box in (a), showing a nominal pitch of ~20.5 nm (indicated by the red dashed lines).

sources operating at 13.5 nm can possess the necessary brightness, stability, and beam quality required to perform IL studies for resist screening at industry-relevant pitch levels.

While these initial experiments using a LM device have demonstrated the utility of HHG-based EUV sources for IL studies, a greater degree of flexibility is needed to make these sources viable for state-of-the-art resist screening and processing. For instance, in the LM setup, the partial reflection of the beam results in an intensity mismatch between the two beams, which reduces the contrast of the resulting interference pattern. The contrast reduction is further compounded by the lack of control over the temporal overlap of the interfering pulses in a LM setup, which also limits the exposure field to a few microns at best. Furthermore, the LM setup is not compatible with resists coated on 300-mm wafers, which limits the ability to perform further processing of the resists once the IL pattern has been written into the resist. To address these challenges, a custom 300-mm compatible IL tool is currently being installed and commissioned at Imec's AttoLab, and is based on a split-and-recombine IL scheme that provides continual tuning of the pitch from 40 nm to 8 nm, with an anticipated exposure fluence of 18 mW/cm^2. As such, this tool will enable high-NA printing emulation of interference patterns on full 300-mm wafers that can then be subjected to feature metrology and etching processes to further increase understanding of how to scale resist property recipes for upcoming high-NA EUV scanners and future technology nodes.

In summary, IL is a versatile method for printing lithographic patterns in photoresists that can provide a complimentary research platform to lithographic patterning by EUV scanners. Interference lithography schemes can thus benefit photoresist material suppliers and researchers by offering an accessible platform for screening photoresist printing capabilities and the study of stochastic defects. However, the limited number of sources of coherent EUV light at 13.5 nm has limited many IL studies to large-scale facilities such as synchrotrons. Thanks to recent advancements in HHG (and the corresponding front-end lasers), HHG-based sources of 13.5-nm EUV light have demonstrated the required coherence, flux, stability, and beam mode quality to be deployed in IL schemes (Fig. 21.22). Furthermore, the small footprint (Fig. 21.7), high up-time, and ease of accessibility of HHG sources further increase their attractiveness for resist screening. As such, we anticipate that HHG-based EUV light sources at 13.5 nm will enable a new avenue for photoresist research that will enhance the capabilities of semiconductor devices in current and future technology nodes.

21.4.6 Studies of EUV-induced chemical dynamics

Ultrafast time-resolved spectroscopies emerged three decades ago with the development of picosecond and femtosecond lasers that deliver ultrashort

light pulses to probe chemical dynamics. For example, the 1999 Nobel Prize in Chemistry was awarded to Ahmed H. Zewail for his pioneering studies of the transition states of chemical reactions in femtochemistry.[128] Femtosecond laser–driven HHG emission can further generate a series of attosecond-duration bursts in the EUV regime with a femtosecond-duration envelope. A further "filtering" in time is possible to generate a single isolated attosecond (as) pulse with <100-as duration by implementing optical gating techniques.[129–131] Combining the use of femtosecond lasers, attosecond pulses from HHG can serve as an ideal spectroscopic tool to further understand and control chemical processes. In fact, a Holy Grail in chemical dynamics includes passively shooting molecular movies (i.e., observing charge motions in real time), as well as actively directing molecular movies (i.e., controlling charge motion on demand).[128]

The characteristic chemical functions of dynamics span from nanosecond down to attosecond timescales. These dynamics include molecular rotations, isomerization, bond vibration, bond breaking and formation, photodissociation and photoionization, charge transfer, and charge migration. In particular, charge migration and coupled electron–nucleus motion of molecules usually happen in a sub-femtosecond timescale.[132,133] Understanding these functions of dynamics is important because many of the light-induced chemical reactions are vital to a large number of biologically relevant processes.[134] For instance, these ultrafast biochemical processes in life include vision, photosynthesis, cellular respiration, DNA damage under radiation, etc. To successfully interrogate the above-mentioned chemical transformations, one has to use both EUV pulses and suitable measurement technologies to capture the process, which involves the detection of photons or charge fragments (electrons and ions). Most of these technologies rely on implementing pump–probe measurement where a pumping pulse excites and starts a chemical process of interest, and then a time-delay probing pulse is followed to interrogate the change of the process. Given the relatively low pulse energy in EUV from HHG, EUV-pump and EUV-probe experiments are still difficult. The typical HHG pulse energy in the nanojoule range, focused into a 10-μm spot, will result in a fluence of $\sim 10^{14}$–10^{15} photon/cm^2; compared with a typical EUV cross-section on the order of a megabarn ($\sim 10^{-18}$ cm^2),[135] photoexcitation is far from saturated, and signal levels are challenging (although not orders-of-magnitude away from practical experiment). Therefore, most experiments to date have combined pump and probe pulses in infrared, visible, UV, and EUV regimes, depending on the experimental design. A more complicated scenario is also possible that uses multiple pulses to perform two-dimensional or multidimensional spectroscopy. Below we provide some examples of how EUV chemical dynamics are studied via different EUV-based spectroscopies.

Direct high-harmonic spectroscopy. In this experimental technique, the gaseous molecular medium used to generate EUV light through the HHG process is also the sample under investigation. The produced EUV properties (e.g., spectra, yields, and polarization) depend on the molecule and its status (e.g., alignment, temperature, ground state, or some excited states/orbitals). As a result, this experimental technique is also called an *in situ* spectroscopy, where the chemical dynamics of the molecules is understood via the interactions between the molecule and the strong field from the driving femtosecond laser. For example, a pump–probe high-harmonic spectroscopy was used to uncover rapid electronic dynamics, where an electron is pulled out of and then pushed back into a vibrating N_2O_4 molecule by an intense laser field, revealing dynamical changes in electronic orbitals.[136] In another example, the Cooper minimum in molecules such as CCl_4, CH_2Cl_2, and trans-$C_2H_2Cl_2$ can be studied using this technique.[137]

Reaction microscope or momentum spectroscopy. Momentum spectroscopies are popular techniques used to detect the total momentum of cations, anions, and electrons, and are often called reaction microscopes because of their source–target interaction. Among these microscopes, the cold target recoil-ion momentum spectroscopy (COLTRIMS) developed in the 1980s provides kinematically complete information on atomic and molecular fragmentation processes by coincident and momentum-resolved detection of recoiling target ions and emitted electrons. Combining COLTRIMS with EUV pumps and infrared probes, scientists identified new dissociation pathways of an EUV-excited N_2 molecule[139] and discovered the creation of electronic Feshbach resonances in EUV-induced O_2 dissociation (Fig. 21.23).[138] In another study, scientists probed the explosion dynamics of a N_2O^+ molecular ion, in a regime dominated by coupled electron–electron and electron–nuclear dynamics and found that the branching ratio of bond breaking can be altered.[140] This important electron–nucleus coupled regime is referred to as non-Born–Oppenheimer dynamics in molecular physics. Along with COLTRIMS, other complementary techniques such as velocity-map imaging (VMI) can also be used to detect photofragments. The VMI technique has a few advantages over COLTRIMS, including a faster data acquisition time of a complete 3D momentum image.

Transient absorption spectroscopy. In addition to measuring photofragments, monitoring photoabsorption can also provide different and complementary time-domain perspectives on EUV-induced processes. In this technique, static EUV absorption spectra are measured before and after the presence of the sample, while dynamic EUV absorption spectra are measured with and without the presence of the delayed pumping pulse(s). Because absorption spectra rely on resonant photoabsorption, care must be taken that the measured results reflect the intrinsic chemical properties under investigation rather that the nonlinear EUV pulse propagation effects through the

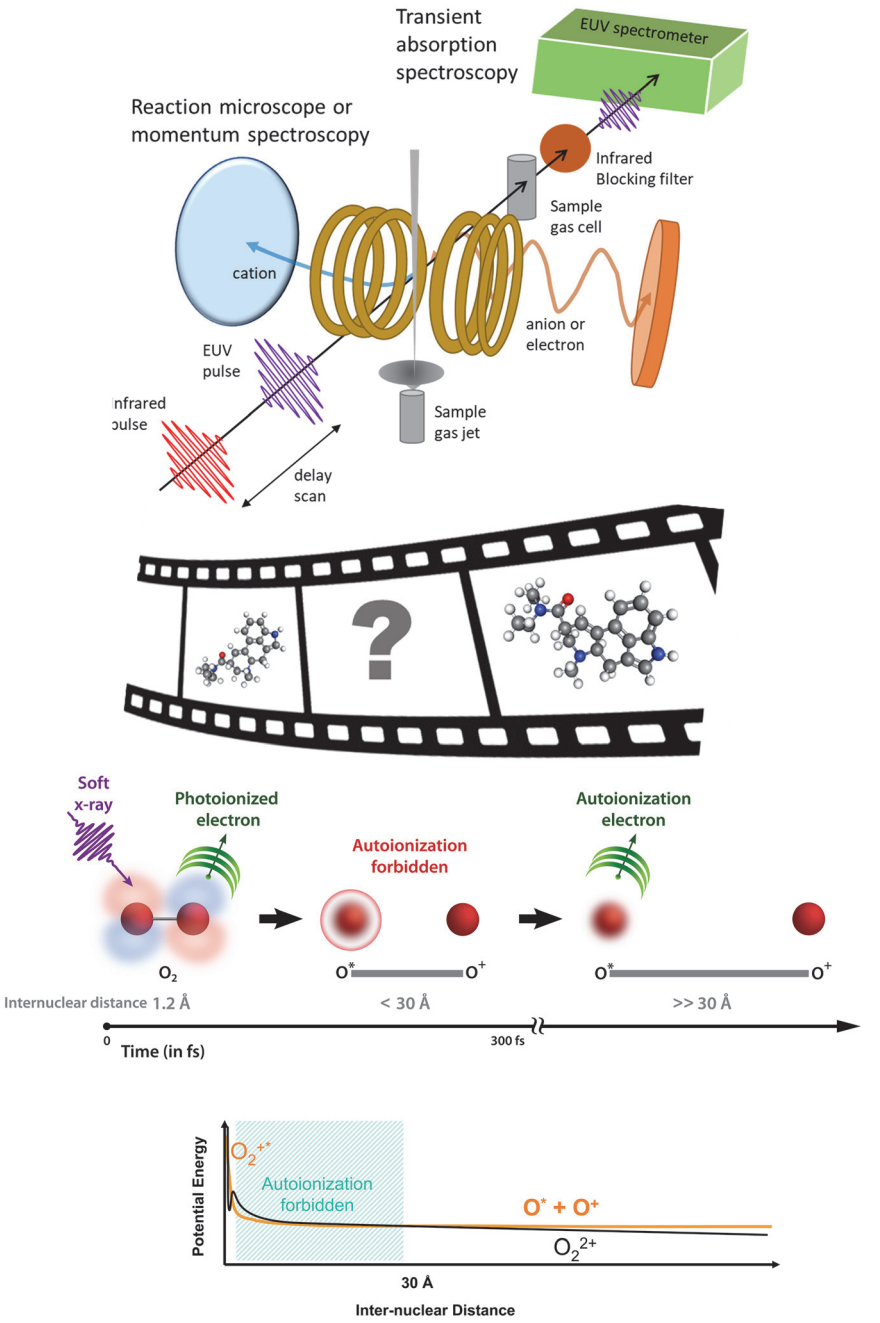

Figure 21.23 (top) Schematic setup of a reaction microscope and transient absorption spectroscopy to study EUV-induced chemical dynamics. (middle) EUV-based pump–probe measurements make it possible to make a "molecular movie" of chemical dynamics. (bottom) Illustration of creation of autoionizing states of atomic oxygen through EUV photodissociation of O_2, followed by passage through a Feshbach resonance. This is an example of chemical dynamics that can be uniquely accessed through EUV interactions and was discovered using pump–probe EUV photoionization in a reaction microscope. (Adapted from Ref. 138).

sample, such as the one identified in noble gas.[141,142] Early adaption of attosecond transient absorption helped scientists reveal a sequence of snapshots that show the oscillatory motion of a valence electron in Xe excited by an infrared pulse and probed by a delayed EUV pulse.[143] On the contrary, EUV pulses can also be used to excite electrons or to prepare atomic/molecular polarizations first, and then a following infrared pulse perturbs the excitation.[144] The perturbation could play many roles, including direct photoionization, quantum-path interference (also called quantum beats) through resonant couplings,[145,146] and transient modification of molecular structures in O_2,[147] to name a few.

21.5 Summary and Conclusions

High-order harmonic light sources have evolved since the 1990s from a physics curiosity to a truly unique tool for new science and, most recently, for technological applications. This evolution was made possible by (1) understanding the physics of the process, (2) using this information to optimize its implementation, and (3) developing a new generation of laser technology expressly suited for this application. As a basic physical process only discovered in the late 1980s, the transition from principle to application is still in its initial stages, with many more experimental techniques and methods to be implemented—and with its broader impact for the most part still to be seen. The new availability of these coherent short-wavelength light sources is also exceedingly timely, as the spatial and temporal scales relevant to our current technology—nanometers and picoseconds/femtoseconds—are an excellent match to this new technology.

Acknowledgments

This work was funded through multiple grants during the time period 1991–2022, most prominently, the National Science Foundation through the ERC, PFC, and STC programs, the Department of Energy Chemical Sciences, Geosciences, & Biosciences program, DARPA, European Union's Horizon 2020 framework, and through IMEC.

References and Note

1. H. Kapteyn, M. Murnane, and I. Christov, "Extreme nonlinear optics: coherent X rays from lasers," *Physics Today* **58**(3), 39–44 (2005).
2. T. T. Luu, Z. Yin, A. Jain, T. Gaumnitz, Y. Pertot, J. Ma, and H. J. Worner, "Extreme-ultraviolet high-harmonic generation in liquids," *Nature Communications* **9**, 10 (2018).

3. S. Ghimire, A. D. DiChiara, E. Sistrunk, P. Agostini, L. F. DiMauro, and D. A. Reis, "Observation of high-order harmonic generation in a bulk crystal," *Nature Physics* **7**(2), 138–141 (2011).
4. P. B. Corkum, "Plasma perspective on strong field multiphoton ionization," *Phys. Rev. Lett*. **71**(13), 1994–1997 (1993).
5. For example, the Spectra-Physics Millennia® and Coherent Verdi Lasers are frequency-doubled 1.06-μm Nd:YVO4 lasers; lasers such as the Spectra-Physics Talon® are frequency tripled to 355 nm, while the Oxide Corp. Frequad Series lasers are frequency quadrupled to 266 nm.
6. A. McPherson, G. Gibson, H. Jara, U. Johann, T. S. Luk, I. A. McIntyre, K. Boyer, and C. K. Rhodes, "Studies of multiphoton production of vacuum ultraviolet-radiation in the rare-gases," *J. Optical Society of America B Optical Physics* **4**(4), 595–601 (1987).
7. R. L. Carman, C. K. Rhodes, and R. F. Benjamin, "Observation of harmonics in the visible and ultraviolet created in CO_2-produced laser plasmas," *Physical Review A* **24**(5), 2649–2663 (1981).
8. M. Ferray, A. L'Huillier, X. F. Li, L. A. Lompre, G. Mainfray, and C. Manus, "Multiple harmonic conversion of 1064-nm radiation in rare-gases," *J. Physics B Atomic Molecular and Optical Physics* **21**(3), L31–L35 (1988).
9. K. C. Kulander and B. W. Shore, "Calculations of multiple-harmonic conversion of 1064-nm radiation in Xe," *Physical Review Letters* **62**(5), 524–526 (1989).
10. J. L. Krause, K. J. Schafer, and K. C. Kulander, "High-order harmonic generation from atoms and ions in the high-intensity regime," *Physical Review Letters* **68**(24), 3535–3538 (1992).
11. J. Zhou, J. Peatross, M. Murnane, and H. Kapteyn, "Enhanced high-harmonic generation using 25 fs laser pulses," *Physical Review Letters* **76**(5), 752–755 (1996).
12. C. Durfee, A. Rundquist, S. Backus, C. Herne, M. Murnane, and H. Kapteyn, "Phase matching of high-order harmonics in hollow waveguides," *Physical Review Letters* **83**(11), 2187–2190 (1999).
13. P. F. Moulton, "Spectroscopic and laser characteristics of Ti-Al_2O_3," *J. Optical Society of America B Optical Physics* **3**(1), 125–133 (1986).
14. S. Backus, C. Durfee, M. Murnane, and H. Kapteyn, "High power ultrafast lasers," *Review of Scientific Instruments* **69**(3), 1207–1223 (1998).
15. Z. Chang, A. Rundquist, H. Wang, I. Christov, H. C. Kapteyn, and M. M. Murnane, "Temporal phase control of soft-x-ray harmonic emission," *Physical Review A* **58**(1), R30–R33 (1998).
16. R. Bartels, S. Backus, E. Zeek, L. Misoguti, G. Vdovin, I. P. Christov, M. M. Murnane, and H. C. Kapteyn, "Shaped-pulse optimization of

coherent emission of high-harmonic soft X-rays," *Nature* **406**(6792), 164–166 (2000).
17. D. E. Spence, P. N. Kean, and W. Sibbett, "60-fsec pulse generation from a self-mode-locked Ti:sapphire laser," *Opt. Lett*. **16**(1), 42–44 (1991).
18. D. Strickland and G. Mourou, "Compression of amplifiend chirped optical pulses," *Optics Communications* **56**(3), 219–221 (1985).
19. M. T. Asaki, C. P. Huang, D. Garvey, J. P. Zhou, H. C. Kapteyn, and M. M. Murnane, "Generation of 11-fs pulses from a self-mode-locked Ti-sapphire laser," *Optics Letters* **18**(12), 977–979 (1993).
20. C. Huang, H. Kapteyn, J. McIntosh, and M. Murnane, "Generation of transform-limited 32-fs pulses from a self-mode-locked Ti-sapphire laser," *Optics Letters* **17**(2), 139–141 (1992).
21. J. Zhou, C. Huang, C. Shi, M. Murnane, and H. Kapteyn, "Generation of 21-fs millijoule-energy pulses by use of Ti-sapphire," *Optics Letters* **19**(2), 126–128 (1994).
22. Z. Chang, A. Rundquist, H. Wang, M. Murnane, and H. Kapteyn, "Generation of coherent soft X rays at 2.7 nm using high harmonics," *Physical Review Letters* **79**(16), 2967–2970 (1997).
23. C. Spielmann, N. H. Burnett, S. Sartania, R. Koppitsch, M. Schnurer, C. Kan, M. Lenzner, P. Wobrauschek, and F. Krausz, "Generation of coherent X-rays in the water window using 5-femtosecond laser pulses," *Science* **278**(5338), 661–664 (1997).
24. N. Bloembergen, *Nonlinear Optics*, World Scientific, River Edge, New Jersey (1996).
25. The Nobel Prize, "The Nobel Prize in Physics 1981," https://www.nobelprize.org/prizes/physics/1981/summary/.
26. P. Balcou, P. Salieres, A. L'Huillier, and M. Lewenstein, "Generalized phase-matching conditions for high harmonics: The role of field-gradient forces," *Physical Review A* **55**(4), 3204–3210 (1997).
27. I. Christov, R. Bartels, H. Kapteyn, and M. Murnane, "Attosecond time-scale intra-atomic phase matching of high harmonic generation," *Physical Review Letters* **86**(24), 5458–5461 (2001).
28. A. Rundquist, C. G. Durfee III, Z. Chang, C. Herne, S. Backus, M. M. Murnane, and H. C. Kapteyn, "Phase-matched generation of coherent soft X-rays," *Science* **280**(5368), 1412–1415 (1998).
29. J. Tate, T. Auguste, H. G. Muller, P. Salieres, P. Agostini, and L. F. DiMauro, "Scaling of wave-packet dynamics in an intense midinfrared field," *Physical Review Letters* **98**(1), 013901 (2007).
30. E. Constant, D. Garzella, P. Breger, E. Mevel, C. Dorrer, C. Le Blanc, F. Salin, and P. Agostini, "Optimizing high harmonic generation in absorbing gases: Model and experiment," *Physical Review Letters* **82**(8), 1668–1671 (1999).

31. A. R. Rundquist, "Phase-matched generation of coherent, ultrafast x-rays using high harmonics," Ph.D. thesis, University of Michigan (1998).
32. T. Popmintchev, M.-C. Chen, D. Popmintchev, P. Arpin, S. Brown, S. Ališauskas, G. Andriukaitis, T. Balčiunas, O. D. Mücke, A. Pugzlys, A. Baltuška, B. Shim, S. E. Schrauth, A. Gaeta, C. Hernández-García, L. Plaja, A. Becker, A. Jaron-Becker, M. M. Murnane, and H. C. Kapteyn, "Bright coherent ultrahigh harmonics in the keV X-ray regime from mid-infrared femtosecond lasers," *Science* **336**(6086), 1287–1291 (2012).
33. D. Popmintchev, C. Hernandez-Garcia, F. Dollar, C. Mancuso, J. A. Perez-Hernandez, M.-C. Chen, A. Hankla, X. Gao, B. Shim, A. L. Gaeta, M. Tarazkar, D. A. Romanov, R. J. Levis, J. A. Gaffney, M. Foord, S. B. Libby, A. Jaron-Becker, A. Becker, L. Plaja, M. M. Murnane, H. C. Kapteyn, and T. Popmintchev, "Ultraviolet surprise: Efficient soft x-ray high-harmonic generation in multiply ionized plasmas," *Science* **350**(6265), 1225–1231 (2015).
34. T. Popmintchev, M. C. Chen, A. Bahabad, M. Gerrity, P. Sidorenko, O. Cohen, I. P. Christov, M. M. Murnane, and H. C. Kapteyn, "Phase matching of high harmonic generation in the soft and hard X-ray regions of the spectrum," *Proceedings of the National Academy of Sciences of the United States of America* **106**(26), 10516–10521 (2009).
35. J. Sutherland, E. Christensen, N. Powers, S. Rhynard, J. Painter, and J. Peatross, "High harmonic generation in a semi-infinite gas cell," *Optics Express* **12**(19), 4430–4436 (2004).
36. A. Libertun, X. Zhang, A. Paul, E. Gagnon, T. Popmintchev, S. Backus, M. Murnane, H. Kapteyn, and I. Christov, "Design of fully spatially coherent extreme-ultraviolet light sources," *Applied Physics Letters* **84**(19), 3903–3905 (2004).
37. A. T. Le, R. R. Lucchese, S. Tonzani, T. Morishita, and C. D. Lin, "Quantitative rescattering theory for high-order harmonic generation from molecules," *Physical Review A* **80**(1), 013401 (2009).
38. J. Peatross, M. V. Fedorov, and K. C. Kulander, "Intensity-dependent phase-matching effects in harmonic generation," *J. Optical Society of America B-Optical Physics* **12**(5), 863–870 (1995).
39. A. Paul, R. A. Bartels, R. Tobey, H. Green, S. Weiman, I. P. Christov, M. M. Murnane, H. C. Kapteyn, and S. Backus, "Quasi-phase-matched generation of coherent extreme-ultraviolet light," *Nature* **421**(6918), 51–54 (2003).
40. I. P. Christov, H. C. Kapteyn, and M. M. Murnane, "Quasi-phase matching of high-harmonics and attosecond pulses in modulated waveguides," *Optics Express* **7**(11), 362–367 (2000).
41. X. H. Zhang, A. L. Lytle, T. Popmintchev, X. B. Zhou, H. C. Kapteyn, M. M. Murnane, and O. Cohen, "Quasi-phase-matching and

quantum-path control of high-harmonic generation using counter-propagating light," *Nature Physics* **3**(4), 270–275 (2007).
42. E. J. Takahashi, H. Hasegawa, Y. Nabekawa, and K. Midorikawa, "High-throughput, high-damage-threshold broadband beam splitter for high-order harmonics in the extreme-ultraviolet region," *Optics Letters* **29**(5), 507–509 (2004).
43. R. W. Falcone and J. Bokor, "Dichroic beam splitter for extreme-ultraviolet and visible radiation," *Optics Letters* **8**(1), 21–23 (1983).
44. Opto Diode Corp., "Photodiodes: Electron, Photon, X-Ray Detectors (AXUV)," https://optodiode.com/photodiodes-axuv-detectors.html.
45. NIST, "Aluminum Oxide EUV Photodetector Transfer Standard," https://www.nist.gov/laboratories/tools-instruments/aluminum-oxide-euv-photodetector-transfer-standard (2015; updated 2022).
46. CXRO, "X-ray Interactions with Matter," http://henke.lbl.gov/optical_constants/ (2015).
47. R. A. Bartels, A. Paul, H. Green, H. C. Kapteyn, M. M. Murnane, S. Backus, I. P. Christov, Y. W. Liu, D. Attwood, and C. Jacobsen, "Generation of spatially coherent light at extreme ultraviolet wavelengths," *Science* **297**(5580), 376–378 (2002).
48. H. Mashiko, A. Suda, and K. Midorikawa, "Focusing coherent soft-x-ray radiation to a micrometer spot size withan intensity of 10^{14} W/cm^2," *Optics Letters* **29**(16), 1927–1929 (2004).
49. Kapteyn-Murnane Laboratories Inc., www.kmlabs.com (2021).
50. Korea IT News, "ESOL Develops Low-Cost System That Can Accelerate the Development of EUV Photoresist," https://english.etnews.com/20190916200001 (2019).
51. Active Fiber Systems GmbH, "High-power XUV beam lines," https://www.afs-jena.de/products/high-power-xuv-beam-lines/.
52. R. Klas, W. Eschen, A. Kirsche, J. Rothhardt, and J. Limpert, "Generation of coherent broadband high photon flux continua in the XUV with a sub-two-cycle fiber laser," *Optics Express* **28**(5), 6188–6196 (2020).
53. G. Andriukaitis, T. Balciunas, S. Alisauskas, A. Pugzlys, A. Baltuska, T. Popmintchev, M. C. Chen, M. M. Murnane, and H. C. Kapteyn, "90 GW peak power few-cycle mid-infrared pulses from an optical parametric amplifier," *Optics Letters* **36**(15), 2755–2757 (2011).
54. R. Butkus, R. Danielius, A. Dubietis, A. Piskarskas, and A. Stabinis, "Progress in chirped pulse optical parametric amplifiers," *Applied Physics B-Lasers and Optics* **79**(6), 693–700 (2004).
55. C. H. Lu, Y. J. Tsou, H. Y. Chen, B. H. Chen, Y. C. Cheng, S. D. Yang, M. C. Chen, C. C. Hsu, and A. H. Kung, "Generation of intense supercontinuum in condensed media," *Optica* **1**(6), 400–406 (2014).

56. C. Rolland and P. B. Corkum, "Compression of high-power optical pulses," *J. Optical Society of America B-Optical Physics* **5**(3), 641–647 (1988).
57. M. Nisoli, S. De Silvestri, and O. Svelto, "Generation of high-energy 10 fs pulses by a new pulse compression technique," *Applied Physics Letters* **68**(20), 2793–2795 (1996).
58. J. R. Fienup, "Phase retrieval algorithms: A comparison," *Applied Optics* **21**(15), 2758–2769 (1982).
59. A. M. Maiden and J. M. Rodenburg, "An improved ptychographical phase retrieval algorithm for diffractive imaging," *Ultramicroscopy* **109**(10), 1256–1262 (2009).
60. H. M. L. Faulkner and J. M. Rodenburg, "Error tolerance of an iterative phase retrieval algorithm for moveable illumination microscopy," *Ultramicroscopy* **103**(2), 153–164 (2005).
61. M. D. Seaberg, B. S. Zhang, D. F. Gardner, E. R. Shanblatt, M. M. Murnane, H. C. Kapteyn, and D. E. Adams, "Tabletop nanometer extreme ultraviolet imaging in an extended reflection mode using coherent Fresnel ptychography," *Optica* **1**(1), 39–44 (2014).
62. B. S. Zhang, D. F. Gardner, M. D. Seaberg, E. R. Shanblatt, H. C. Kapteyn, M. M. Murnane, and D. E. Adams, "High contrast 3D imaging of surfaces near the wavelength limit using tabletop EUV ptychography," *Ultramicroscopy* **158**, 98–104 (2015).
63. M. D. Seaberg, D. E. Adams, E. L. Townsend, D. A. Raymondson, W. F. Schlotter, Y. Liu, C. S. Menoni, L. Rong, C.-C. Chen, J. Miao, H. C. Kapteyn, and M. M. Murnane, "Ultrahigh 22 nm resolution coherent diffractive imaging using a desktop 13 nm high harmonic source," *Optics Express* **19**(23), 22470–22479 (2011).
64. C. L. Porter, M. Tanksalvala, M. Gerrity, G. Miley, X. S. Zhang, C. Bevis, E. Shanblatt, R. Karl, M. M. Murnane, D. E. Adams, and H. C. Kapteyn, "General-purpose, wide field-of-view reflection imaging with a tabletop 13 nm light source," *Optica* **4**(12), 1552–1557 (2017).
65. Y. Nagata, T. Harada, T. Watanabe, H. Kinoshita, and K. Midorikawa, "At wavelength coherent scatterometry microscope using high-order harmonics for EUV mask inspection," *International Journal of Extreme Manufacturing* **1**(3), 032001 (2019).
66. I. Mochi, P. Helfenstein, I. Mohacsi, R. Rajendran, D. Kazazis, S. Yoshitake, and Y. Ekinci, "RESCAN: an actinic lensless microscope for defect inspection of EUV reticles," *J. Micro/Nanolithography, MEMS, and MOEMS* **16**(4), 041003 (2017) [doi: 10.1117/1.JMM.16.4.041003].
67. T. Harada, H. Hashimoto, T. Amano, H. Kinoshita, and T. Watanabe, "Actual defect observation results of an extreme-ultraviolet blank mask

by coherent diffraction imaging," *Applied Physics Express* **9**(3), 035202 (2016).
68. D. F. Gardner, M. Tanksalvala, E. R. Shanblatt, X. S. Zhang, B. R. Galloway, C. L. Porter, R. Karl, C. Bevis, D. E. Adams, H. C. Kapteyn, M. Murnane, and G. F. Mancini, "Subwavelength coherent imaging of periodic samples using a 13.5 nm tabletop high-harmonic light source," *Nature Photonics* **11**(4), 259– (2017).
69. R. M. Karl, G. F. Mancini, J. L. Knobloch, T. D. Frazer, J. N. Hernandez-Charpak, B. Abad, D. F. Gardner, E. R. Shanblatt, M. Tanksalvala, C. L. Porter, C. S. Bevis, D. E. Adams, H. C. Kapteyn, and M. M. Murnane, "Full-field imaging of thermal and acoustic dynamics in an individual nanostructure using tabletop high harmonic beams," *Science Advances* **4**(10), 7 (2018).
70. Y. W. Kim, D. G. Woo, and J. Ahn, "Performance of extreme-ultraviolet coherent scattering miscrope," *J. Nanoscience and Nanotechnology* **19**(10), 6463–6467 (2019)
71. E. R. Shanblatt, C. L. Porter, D. F. Gardner, G. F. Mancini, R. M. Karl, M. D. Tanksalvala, C. S. Bevis, V. H. Vartanian, H. C. Kapteyn, D. E. Adams, and M. M. Murnane, "Quantitative chemically specific coherent diffractive imaging of reactions at buried interfaces with few nanometer precision," *Nano Letters* **16**(9), 5444–5450 (2016).
72. M. Tanksalvala, C. L. Porter, Y. Esashi, B. Wang, N. W. Jenkins, Z. Zhang, G. P. Miley, J. L. Knobloch, B. McBennett, N. Horiguchi, S. Yazdi, J. Zhou, M. N. Jacobs, C. S. Bevis, R. M. Karl, P. Johnsen, D. Ren, L. Waller, D. E. Adams, S. L. Cousin, C.-T. Liao, J. Miao, M. Gerrity, H. C. Kapteyn, and M. M. Murnane, "Nondestructive, high-resolution, chemically specific 3D nanostructure characterization using phase-sensitive EUV imaging reflectometry," *Science Advances* **7**(5), eabd9667 (2021).
73. K. Esfarjani, G. Chen, and H. T. Stokes, "Heat transport in silicon from first-principles calculations," *Physical Review B* **84**(8), 11 (2011).
74. G. Chen, "Nonlocal and nonequilibrium heat conduction in the vicinity of nanoparticles," *J. Heat Transfer-Transactions of the ASME* **118**(3), 539–545 (1996).
75. J. Cuffe, J. K. Eliason, A. A. Maznev, K. C. Collins, J. A. Johnson, A. Shchepetov, M. Prunnila, J. Ahopelto, C. M. S. Torres, G. Chen, and K. A. Nelson, "Reconstructing phonon mean-free-path contributions to thermal conductivity using nanoscale membranes," *Physical Review B* **91**(24), 6 (2015).
76. M. Asheghi, Y. K. Leung, S. S. Wong, and K. E. Goodson, "Phonon-boundary scattering in thin silicon layers," *Applied Physics Letters* **71**(13), 1798–1800 (1997).

77. A. I. Hochbaum, R. K. Chen, R. D. Delgado, W. J. Liang, E. C. Garnett, M. Najarian, A. Majumdar, and P. D. Yang, "Enhanced thermoelectric performance of rough silicon nanowires," *Nature* **451**, 163–167 (2008).
78. A. J. Minnich, J. A. Johnson, A. J. Schmidt, K. Esfarjani, M. S. Dresselhaus, K. A. Nelson, and G. Chen, "Thermal conductivity spectroscopy technique to measure phonon mean free paths," *Physical Review Letters* **107**(9), 095901 (2011).
79. J. A. Johnson, J. K. Eliason, A. A. Maznev, T. F. Luo, and K. A. Nelson, "Non-diffusive thermal transport in GaAs at micron length scales," *J. Applied Physics* **118**(15), 155104 (2015).
80. Y. K. Koh and D. G. Cahill, "Frequency dependence of the thermal conductivity of semiconductor alloys," *Physical Review B* **76**(7), 075207 (2007).
81. Y. J. Hu, L. P. Zeng, A. J. Minnich, M. S. Dresselhaus, and G. Chen, "Spectral mapping of thermal conductivity through nanoscale ballistic transport," *Nature Nanotechnology* **10**(8), 701–706 (2015).
82. R. B. Wilson and D. G. Cahill, "Anisotropic failure of Fourier theory in time-domain thermoreflectance experiments," *Nature Communications* **5**, 5075 (2014).
83. M. E. Siemens, Q. Li, R. G. Yang, K. A. Nelson, E. H. Anderson, M. M. Murnane, and H. C. Kapteyn, "Quasi-ballistic thermal transport from nanoscale interfaces observed using ultrafast coherent soft X-ray beams," *Nature Materials* **9**(1), 26–30 (2010).
84. M. M. Waldrop, "The chips are down for Moore's law," *Nature* **530**(7589), 144–147 (2016).
85. M. I. Hussein, C. N. Tsai, and H. Honarvar, "Thermal conductivity reduction in a nanophononic metamaterial versus a nanophononic crystal: a review and comparative analysis," *Advanced Functional Materials* **30**(8), 1906718 (2020).
86. L. Qiu, N. Zhu, Y. H. Feng, E. E. Michaelides, G. Zyla, D. W. Jing, X. X. Zhang, P. M. Norris, C. N. Markides, and O. Mahian, "A review of recent advances in thermophysical properties at the nanoscale: From solid state to colloids," *Physics Reports-Review Section of Physics Letters* **843**, 1–81 (2020).
87. K. M. Hoogeboom-Pot, J. N. Hernandez-Charpak, X. K. Gu, T. D. Frazer, E. H. Anderson, W. L. Chao, R. W. Falcone, R. G. Yang, M. M. Murnane, H. C. Kapteyn, and D. Nardi, "A new regime of nanoscale thermal transport: Collective diffusion increases dissipation efficiency," *Proceedings of the National Academy of Sciences of the United States of America* **112**(16), 4846–4851 (2015).
88. T. D. Frazer, J. L. Knobloch, K. M. Hoogeboom-Pot, D. Nardi, W. Chao, R. W. Falcone, M. M. Murnane, H. C. Kapteyn, and J. N. Hernandez-Charpak, "Engineering nanoscale thermal transport:

size- and spacing-dependent cooling of nanostructures," *Physical Review Applied* **11**(2), 024042 (2019).

89. A. Beardo, J. L. Knobloch, L. Sendra, J. Bafaluy, T. D. Frazer, W. Chao, J. N. Hernandez-Charpak, H. C. Kapteyn, B. Abad, M. M. Murnane, F. X. Alvarez, and J. Camacho, "A general and predictive understanding of thermal transport from 1D- and 2D-confined nanostructures: Theory and Experiment," *ACS Nano* **15**(8), 13019–13030 (2021).
90. R. I. Tobey, M. E. Siemens, O. Cohen, M. M. Murnane, H. C. Kapteyn, and K. A. Nelson, "Ultrafast extreme ultraviolet holography: dynamic monitoring of surface deformation," *Optics Letters* **32**(3), 286–288 (2007).
91. D. Naumenko, R. Mincigrucci, M. Altissimo, L. Foglia, A. Gessini, G. Kurdi, I. Nikolov, E. Pedersoli, E. Principi, A. Simoncig, M. Kiskinova, C. Masciovecchio, F. Capotondi, and F. Bencivenga, "Thermoelasticity of nanoscale silicon carbide membranes excited by extreme ultraviolet transient gratings: implications for mechanical and thermal management," *ACS Applied Nano Materials* **2**(8), 5132–5139 (2019).
92. H. J. Eichler, P. Günter, and D. W. Pohl, *Laser-Induced Dynamic Gratings, Springer Series in Optical Sciences* **50**, Springer-Verlag, Berlin Heidelberg (1986).
93. R. I. Tobey, M. E. Siemens, M. M. Murnane, H. C. Kapteyn, D. H. Torchinsky, and K. A. Nelson, "Transient grating measurement of surface acoustic waves in thin metal films with extreme ultraviolet radiation," *Applied Physics Letters* **89**(9), 191108 (2006).
94. A. A. Maznev, F. Bencivenga, A. Cannizzo, F. Capotondi, R. Cucini, R. A. Duncan, T. Feurer, T. D. Frazer, L. Foglia, H. M. Frey, H. Kapteyn, J. Knobloch, G. Knopp, C. Masciovecchio, R. Mincigrucci, G. Monaco, M. Murnane, I. Nikolov, E. Pedersoli, A. Simoncig, A. Vega-Flick, and K. A. Nelson, "Generation of coherent phonons by coherent extreme ultraviolet radiation in a transient grating experiment," *Applied Physics Letters* **113**(22), 221905 (2018).
95. F. Bencivenga, R. Mincigrucci, F. Capotondi, L. Foglia, D. Naumenko, A. A. Maznev, E. Pedersoli, A. Simoncig, F. Caporaletti, V. Chiloyan, R. Cucini, F. Dallari, R. A. Duncan, T. D. Frazer, G. Gaio, A. Gessini, L. Giannessi, S. Huberman, H. Kapteyn, J. Knobloch, G. Kurdi, N. Mahne, M. Manfredda, A. Martinelli, M. Murnane, E. Principi, L. Raimondi, S. Spampinati, C. Spezzani, M. Trovo, M. Zangrando, G. Chen, G. Monaco, K. A. Nelson, and C. Masciovecchio, "Nanoscale transient gratings excited and probed by extreme ultraviolet femtosecond pulses," *Science Advances* **5**(7), 5805 (2019).

96. H. Honarvar, J. L. Knobloch, T. D. Frazer, B. Abad, B. McBennett, M. I. Hussein, H. C. Kapteyn, M. M. Murnane, and J. N. Hernandez-Charpak, "Direct thermal chanelling: A phenomenon trigggered by tight packing of heat sources," *Proceedings of the National Academy of Sciences of the United States of America* **118**(40), e2109056118 (2021).
97. S. W. King, H. Simka, D. Herr, H. Akinaga, and M. Garner, "Research updates: The three M's (materials, metrology, and modeling) together pave the path to future nanoelectronic technologies," *Applied Materials* **1**(4), 040701 (2013).
98. J. N. Hernandez-Charpak, K. M. Hoogeboom-Pot, Q. Li, T. D. Frazer, J. L. Knobloch, M. Tripp, S. W. King, E. H. Anderson, W. L. Chao, M. M. Mumane, H. C. Kapteyn, and D. Nardit, "Full characterization of the mechanical properties of 11-50 nm ultrathin films: influence of network connectivity on Poisson's ratio," *Nano Letters* **17**(4), 2178–2183 (2017).
99. J. Hay and B. Crawford, "Measuring substrate-independent modulus of thin films," *J. Materials Research* **26**(6), 727–738 (2011).
100. B. Zhou and B. C. Prorok, "A new paradigm in thin film indentation," *J. Materials Research* **25**(9), 1671–1678 (2010).
101. A. Link, R. Sooryakumar, R. S. Bandhu, and G. A. Antonelli, "Brillouin light scattering studies of the mechanical properties of ultrathin low-k dielectric films," *J. Applied Physics* **100**(1), 103507 (2006).
102. O. Matsuda, M. C. Larciprete, R. Li Voti, and O. B. Wright, "Fundamentals of picosecond laser ultrasonics," *Ultrasonics* **56**, 3–20 (2015).
103. J. Zizka, S. King, A. Every, and R. Sooryakumar, "Acoustic phonons and mechanical properties of ultra-thin porous low-k films: a surface Brillouin scattering study," *J. Electronic Materials* **47**(7), 3942–3950 (2018).
104. M. G. Beghi, C. E. Bottani, A. L. Bassi, P. M. Ossi, B. K. Tanner, A. C. Ferrari, and J. Robertson, "Measurement of the elastic constants of nanometer-thick films," *Materials Science & Engineering C-Biomimetic and Supramolecular Systems* **19**(1–2), 201–204 (2002).
105. H. Ogi, M. Fujii, N. Nakamura, T. Shagawa, and M. Hirao, "Resonance acoustic-phonon spectroscopy for studying elasticity of ultrathin films," *Applied Physics Letters* **90**(19), 191906 (2007).
106. D. Nardi, F. Banfi, C. Giannetti, B. Revaz, G. Ferrini, and F. Parmigiani, "Pseudosurface acoustic waves in hypersonic surface phononic crystals," *Physical Review B* **80**(10), 104119 (2009).
107. T. D. Frazer, J. L. Knobloch, J. N. Hernandez-Charpak, K. M. Hoogeboom-Pot, D. Nardi, S. Yazdi, W. L. Chao, E. H. Anderson, M. K. Tripp, S. W. King, H. C. Kapteyn, M. M. Murnane, and B. Abad, "Full characterization of ultrathin 5-nm low-k dielectric

bilayers: Influence of dopants and surfaces on the mechanical properties," *Physical Review Materials* **4**(7), 073603 (2020).
108. K. M. Hoogeboom-Pot, E. Turgut, J. N. Hernandez-Charpak, J. M. Shaw, H. C. Kapteyn, M. M. Murnane, and D. Nardi, "Nondestructive measurement of the evolution of layer-specific mechanical properties in sub-10 nm bilayer films," *Nano Letters* **16**(8), 4773–4778 (2016).
109. B. Abad, J. Knobloch, T. D. Frazer, J. N. Hernandez-Charpak, H. Y. Cheng, A. J. Grede, N. C. Giebink, T. E. Mallouk, P. Mahale, N. N. Nova, A. A. Tomaschke, V. L. Ferguson, V. H. Crespi, V. Gopalan, H. C. Kapteyn, J. V. Badding, and M. M. Murnane, "Nondestructive measurements of the mechanical and structural properties of nanostructured metalattices," *Nano Letters* **20**(5), 3306–3312 (2020).
110. M. E. Siemens, Q. Li, M. M. Murnane, H. C. Kapteyn, R. Yang, E. H. Anderson, and K. A. Nelson, "High-frequency surface acoustic wave propagation in nanostructures characterized by coherent extreme ultraviolet beams," *Applied Physics Letters* **94**(9), 093103 (2009).
111. D. Nardi, M. Travagliati, M. E. Siemens, Q. Li, M. M. Murnane, H. C. Kapteyn, G. Ferrini, F. Parmigiani, and F. Banfi, "Probing thermomechanics at the nanoscale: impulsively excited pseudosurface acoustic waves in hypersonic phononic crystals," *Nano Letters* **11**(10), 4126–4133 (2011).
112. Q. Li, K. Hoogeboom-Pot, D. Nardi, M. M. Murnane, H. C. Kapteyn, M. E. Siemens, E. H. Anderson, O. Hellwig, E. Dobisz, B. Gurney, R. Yang, and K. A. Nelson, "Generation and control of ultrashort-wavelength two-dimensional surface acoustic waves at nanoscale interfaces," *Physical Review B* **85**(19), 195431 (2012).
113. E. Hendrickx, R. Gronheid, J. Hermans, G. Lorusso, P. Foubert, I. Pollentier, A. M. Goethals, R. Jonckheere, G. Vandenberghe, and K. Ronse, "Readiness of EUV lithography for insertion into manufacturing: The IMEC EUV Program," *J. Photopolymer Science and Technology* **26**(5), 587–593 (2013).
114. E. van Setten, G. Bottiglieri, J. McNamara, J. van Schoot, K. Troost, J. Zekry, T. Fliervoet, S. Hsu, J. Zimmermann, M. Roesch, B. Bilski, and P. Graeupner, "High NA EUV lithography: Next step in EUV imaging," *Proc. SPIE* **10957**, 1095709 (2019) [doi: 10.1117/12.2514952].
115. T. Manouras and P. Argitis, "High sensitivity resists for EUV lithography: a review of material design strategies and performance results," *Nanomaterials* **10**(8), 1593 (2020).
116. A. Lio, "EUV photoresists: A progress report and future prospects," *Synchrotron Radiation News* **32**(4), 9–14 (2019).

117. D. De Simone, Y. Vesters, and G. Vandenberghe, "Photoresists in extreme ultraviolet lithography (EUVL)," *Advanced Optical Technologies* **6**(3-4), 163–172 (2017).
118. N. Mojarad, J. Gobrecht, and Y. Ekinci, "Interference lithography at EUV and soft X-ray wavelengths: Principles, methods, and applications," *Microelectronic Engineering* **143**, 55–63 (2015).
119. V. Auzelyte, C. Dais, P. Farquet, D. Grutzmacher, L. J. Heyderman, F. Luo, S. Olliges, C. Padeste, P. K. Sahoo, T. Thomson, A. Turchanin, C. David, and H. H. Solak, "Extreme ultraviolet interference lithography at the Paul Scherrer Institut," *J. Micro-Nanolithography MEMS, MOEMS* **8**(2), 021204 (2009) [doi: 10.1117/1.3116559].
120. E. Buitrago, O. Yildirim, C. Verspaget, N. Tsugama, R. Hoefnagels, G. Rispens, and Y. Ekinci, "Evaluation of EUV resist performance using interference lithography," *Proc. SPIE* **9422**, 94221S (2015) [doi: 10.1117/12.2085803].
121. X. Wang, L.-T. Tseng, T. Allenet, I. Mochi, M. Vockenhuber, C.-K. Yeh, L. van Lent-Protasova, J. Garcia Santaclara, R. Custers, and Y. Ekinci, "Progress in EUV resists status towards high-NA EUV lithography," *Proc. SPIE* **11323**, 113230C (2020) [doi: 10.1117/12.2551886].
122. A. Robinson, R. Lawson, Eds., *Materials and Processes for Next Generation Lithography, Frontiers of Nanoscience* **11**, Elsevier, Amsterdam (2016).
123. S. Gunnell, "Energetiq Technology: EUV sources from Energetiq," *Proc. SPIE* **PV20EX**, PV20EX09 (2020) [doi: 10.1117/12.2584908].
124. Z. Andreic, S. S. Ellwi, S. Pleslic, and H. J. Kunze, "Performance of the 13.5 nm PVC capillary discharge EUV source," *Physics Letters A* **335**(5–6), 430–434 (2005).
125. S. L. Cousin, C. Bargsten, E. Rinard, R. Ward, E. Hosler, B. Petersen, H. Kapteyn, P. Vanelderen, J. Petersen, and P. van der Heide, "A laboratory light source for ultrafast kinetics of EUV exposure processes and ultra-small pitch lithography," in *Conference on Lasers and Electro-Optics*, OSA Technical Digest, paper ATh1.K.5 (2020).
126. H. S. Kim, P. Baksh, M. Odstrcil, M. Miszczak, J. G. Frey, L. Juschkin, and W. S. Brocklesby, "Lloyd's mirror interference lithography with EUV radiation from a high-harmonic source," *Applied Physics Express* **9**(7), 076701 (2016).
127. K. Dorney, S. Castellanos, E. Larsen, F. Holzmeier, D. Singh, N. Vandenbroeck, D. De Simone, P. De Schepper, A. VaglioPret, C. Bargsten, S. Cousin, D. Raymondson, E. Rinard, R. Ward, H. Kaptyen, T. Nuytten, P. Van der Heide, and J. Petersen, "Lloyd's mirror interference lithography below a 22-nm pitch with an accessible,

tabletop, 13.5 nm high-harmonic EUV source," *Proc. SPIE* **11610**, 1161011 [Presentation] (2021) [doi: 10.1117/12.2595048].
128. A. H. Zewail, "Femtochemistry: Atomic-scale dynamics of the chemical bond," *J. Physical Chemistry A* **104**(24), 5660–5694 (2000).
129. M. Chini, K. Zhao, and Z. H. Chang, "The generation, characterization and applications of broadband isolated attosecond pulses," *Nature Photonics* **8**(3), 178–186 (2014).
130. I. Christov, M. Murnane, and H. Kapteyn, "High-harmonic generation of attosecond pulses in the 'single-cycle' regime," *Physical Review Letters* **78**(7), 1251–1254 (1997).
131. L. Young, K. Ueda, M. Guhr, P. H. Bucksbaum, M. Simon, S. Mukamel, N. Rohringer, K. C. Prince, C. Masciovecchio, M. Meyer, A. Rudenko, D. Rolles, C. Bostedt, M. Fuchs, D. A. Reis, R. Santra, H. Kapteyn, M. Murnane, H. Ibrahim, F. Legare, M. Vrakking, M. Isinger, D. Kroon, M. Gisselbrecht, A. L'Huillier, H. J. Worner, and S. R. Leone, "Roadmap of ultrafast x-ray atomic and molecular physics," *J. Physics B-Atomic Molecular and Optical Physics* **51**(3), 032003 (2018).
132. P. M. Kraus, B. Mignolet, D. Baykusheva, A. Rupenyan, L. Horny, E. F. Penka, G. Grassi, O. I. Tolstikhin, J. Schneider, F. Jensen, L. B. Madsen, A. D. Bandrauk, F. Remacle, and H. J. Worner, "Measurement and laser control of attosecond charge migration in ionized iodoacetylene," *Science* **350**(6262), 790–795 (2015).
133. A. Palacios, A. Gonzalez-Castrillo, and F. Martin, "Molecular interferometer to decode attosecond electron-nuclear dynamics," *Proceedings of the National Academy of Sciences of the United States of America* **111**(11), 3973–3978 (2014).
134. M. Nisoli, P. Decleva, F. Calegari, A. Palacios, and F. Martin, "Attosecond electron dynamics in molecules," *Chemical Reviews* **117**(16), 10760–10825 (2017).
135. J. J. Yeh and I. Lindau, "Atomic subshell photoionization cross sections and asymmetry parameters: $1 \leq Z \leq 103$," *Atomic Data and Nuclear Data Tables* **32**(1), 1–155 (1986).
136. W. Li, X. Zhou, R. Lock, S. Patchkovskii, A. Stolow, H. C. Kapteyn, and M. M. Murnane, "Time-resolved dynamics in N_2O_4 probed using high harmonic generation," *Science* **322**(5905), 1207–1211 (2008).
137. M. C. H. Wong, A. T. Le, A. F. Alharbi, A. E. Boguslavskiy, R. R. Lucchese, J. P. Brichta, C. D. Lin, and V. R. Bhardwaj, "High harmonic spectroscopy of the Cooper minimum in molecules," *Physical Review Letters* **110**(3), 033006 (2013).
138. A. S. Sandhu, E. Gagnon, R. Santra, V. Sharma, W. Li, P. Ho, P. Ranitovic, C. L. Cocke, M. M. Murnane, and H. C. Kapteyn,

"Observing the creation of electronic Feshbach resonances in soft X-ray-induced O_2 dissociation," *Science* **322**(5904), 1081–1085 (2008).
139. E. Gagnon, P. Ranitovic, X. M. Tong, C. L. Cocke, M. M. Murnane, H. C. Kapteyn, and A. S. Sandhu, "Soft X-ray-driven femtosecond molecular dynamics," *Science* **317**(5843), 1374–1378 (2007).
140. X. Zhou, P. Ranitovic, C. W. Hogle, J. H. D. Eland, H. C. Kapteyn, and M. M. Murnane, "Probing and controlling non-Born-Oppenheimer dynamics in highly excited molecular ions," *Nature Physics* **8**(3), 232–237 (2012).
141. C. T. Liao, A. Sandhu, S. Camp, K. J. Schafer, and M. B. Gaarde, "Beyond the single-atom response in absorption line shapes: probing a dense, laser-dressed helium gas with attosecond pulse trains," *Physical Review Letters* **114**(14), 143002 (2015).
142. C. T. Liao, A. Sandhu, S. Camp, K. J. Schafer, and M. B. Gaarde, "Attosecond transient absorption in dense gases: Exploring the interplay between resonant pulse propagation and laser-induced line-shape control," *Physical Review A* **93**(3), 033405 (2016).
143. E. Goulielmakis, Z. H. Loh, A. Wirth, R. Santra, N. Rohringer, V. S. Yakovlev, S. Zherebtsov, T. Pfeifer, A. M. Azzeer, M. F. Kling, S. R. Leone, and F. Krausz, "Real-time observation of valence electron motion," *Nature* **466**(7307), 739–743 (2010).
144. C.-T. Liao and A. Sandhu, "XUV transient absorption spectroscopy: probing laser-perturbed dipole polarization in single atom, macroscopic, and molecular regimes," *Photonics* **4**(1), 17 (2017).
145. S. H. Chen, M. Wu, M. B. Gaarde, and K. J. Schafer, "Quantum interference in attosecond transient absorption of laser-dressed helium atoms," *Physical Review A* **87**(3), 033408 (2013).
146. N. Harkema, J. E. Baekhoj, C. T. Liao, M. B. Gaarde, K. J. Schafer, and A. Sandhu, "Controlling attosecond transient absorption with tunable, non-commensurate light fields," *Optics Letters* **43**(14), 3357–3360 (2018).
147. C. T. Liao, X. Li, D. J. Haxton, T. N. Rescigno, R. R. Lucchese, C. W. McCurdy, and A. Sandhu, "Probing autoionizing states of molecular oxygen with XUV transient absorption: Electronic-symmetry-dependent line shapes and laser-induced modifications," *Physical Review A* **95**(4), 043427 (2017).

Henry C. Kapteyn is Professor of Physics at the University of Colorado at Boulder and at JILA, and also serves as CTO of the spin-off company Kapteyn-Murnane Laboratories Inc. He received his B.S. degree in physics from Harvey Mudd College in 1982, his M.A. from Princeton University in 1984, and a Ph.D. in physics from University of California Berkeley in 1989. He and his wife and long-term collaborator, Margaret Murnane, are well known for their research in femtosecond lasers, and for understanding how to coherently upconvert this light to make a "tabletop x-ray laser" that generates ultrashort bursts of short-wavelength light. In recent years, they have applied this source to pioneering studies of atomic, molecular, and material studies at short length- and timescales. He has published several hundred papers on topics ranging from laser science and engineering to materials to nanoimaging. He is a member of the U.S. National Academy of Sciences, the American Academy of Arts and Sciences, and is a fellow of the American Physical Society, Optica, and the American Association for the Advancement of Science. His awards include the Ahmed Zewail Award of the ACS, the R.W. Wood Prize of the OSA, the Arthur Schawlow Prize of the APS, and the Benjamin Franklin Medal in Physics. Since 2015, his time has been primarily spent at KMLabs, spearheading the efforts to commercialize coherent EUV laser technologies and novel ultrafast lasers.

Margaret M. Murnane is a Distinguished Professor of Physics at the University of Colorado and a Fellow of JILA. She received her B.S. and M.S. degrees at University College, Cork, Ireland, and a Ph.D. (1989) from UC Berkeley. Her work has led to both major practical advances in the technology of ultrashort-pulse lasers and the conception of the field of *ultrafast x-ray science*. By understanding how to use femtosecond-pulse lasers ($1\,\text{fs} = 10^{-15}\,\text{s}$) to manipulate atomic dynamics on its most-fundamental, attosecond ($10^{-18}\,\text{s}$) timescale, her group showed how to generate bright x-ray beams using high harmonic generation. In recent years, her work has increasingly emphasized the application of this new tool for materials and nanotechnology applications. Margaret's work has been recognized through numerous honors, including a MacArthur Foundation Fellowship (2000), the Frederick Ives Medal (Optica, 2017), the Benjamin Franklin Medal in Physics (2021), and the Isaac Newton Medal (Institute of Physics UK, 2022). She is a member of the National Academy of Sciences and the American Academy of Arts and Sciences, and a fellow of the APS, OSA, and AAAS. In Ireland, she received the Boyle Medal (2011) and is an Honorary Member of the Irish Academy of Sciences (2013). Margaret is also very active in the promotion of diversity in the sciences,

having participated in and chaired both the APS Committee on the Status of Women in Physics, and the President's Committee for the National Medals of Science.

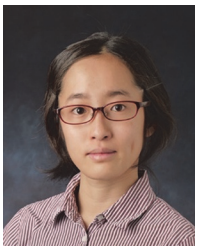

Yuka Esashi is a graduate student at JILA and the University of Colorado Boulder in the research group headed by Professors Margaret Murnane and Henry Kapteyn. She received her B.A. in Physics from Reed College in 2017 and her M.S. in Physics from the University of Colorado Boulder in 2019. She was the recipient of the Nick Cobb Memorial Scholarship from SPIE and Mentor Graphics in 2021. Her current research focuses on using tabletop coherent extreme-ultraviolet light for semiconductor and nanotechnology metrology and imaging applications. She is also a part of the STROBE NSF Science and Technology Center, led by Prof. Margaret Murnane, dedicated to advancing imaging science technologies and capabilities.

Michael D. Tanksalvala is a graduate student at JILA and the University of Colorado Boulder in the research group headed by Professors Margaret Murnane and Henry Kapteyn. He received his B.S. degree (2014) from the University of Colorado in engineering physics and electrical and computer engineering. His current research focuses on developing novel coherent diffractive imaging approaches for material-sensitive imaging. He is also a part of the STROBE NSF Science and Technology Center, led by Prof. Margaret Murnane, dedicated to advancing imaging science technologies and capabilities.

Joshua L. Knobloch is a postdoctoral associate at JILA and the University of Colorado Boulder in the research group headed by Professors Margaret Murnane and Henry Kapteyn. He received his B.S. degree (2014) from Purdue University in physics honors and core mathematics and his Ph.D. (2020) from the University of Colorado Boulder in physics. He was the recipient of the Semiconductor Research Corporation Education Alliance graduate research fellowship. His current research focuses on utilizing tabletop coherent sources of extreme-ultraviolet light to gain novel insight into heat flow, mechanical properties, and energy transport in complex nanostructured materials. He is also a part of the STROBE NSF Science and Technology Center, led by Prof. Margaret Murnane, dedicated to advancing imaging science technologies and capabilities.

Chen-Ting Liao is a senior research associate at JILA and the University of Colorado Boulder, and the assistant director of research and knowledge transfer at STROBE, NSF Science and Technology Center. He received his Ph.D. in optical sciences at the University of Arizona in 2017. He received his M.S. degree from the University of Arizona and another M.S. degree and a B.A. degree from the National Central University in Taiwan. He was the finalist of both the APS Carl E. Anderson Division of Laser Science Dissertation Award and the WAGS/ProQuest Innovation in Technology Award. His current research interests are developing and using coherent light sources from infrared to x-ray regimes. Taking advantage of both tabletop (laser-driven high-order harmonic generation) and facility scale (synchrotron) EUV and x-ray sources, his work also investigates quantum effects and light–matter interactions in atoms, molecules, and materials.

Daniel D. Hickstein is a research scientist at KMLabs in Boulder, Colorado. He completed his postdoctoral work in the Time and Frequency Division at NIST, developing new types of on-chip frequency combs. He earned a Ph.D. at the University of Colorado studying high harmonic generation and photoelectron/photoion spectroscopy. He earned a M.S. degree in Physics from the University of Cambridge and a B.S. degree in Chemistry from Pomona College.

Clayton Bargsten is a Systems Engineer at Kapteyn-Murnane Laboratories Inc. He received his B.S. in Physics and Engineering Science in 2012 and his M.S. in Electrical Engineering in 2016. His most recent work has been in collaboration with Imec on the development of an interference lithography system for 300-mm wafers using 13.5-nm light from HHG sources to facilitate faster and more economical development of semiconductor photoresists.

Kevin Dorney is a postdoctoral researcher and MSCA fellow in AttoLab at Imec in Leuven, Belgium. He received B.S. degrees in Biology and Chemistry (2012) as well as an M.S. in Chemistry (2014) from Wright State University (Ohio, USA). In 2019, he earned a Ph.D. in Chemical Physics under the supervision of Profs. Margaret Murnane and Henry Kapteyn in JILA at the University of Colorado Boulder, specializing in HHG-based generation of structured EUV beams with tailored spin and orbital angular momentum. His current research interests involve the deployment of bright, coherent 13.5-nm EUV light from

HHG systems to investigate the ultrafast radiochemistry of the EUV exposure mechanism in photoresists, as well as the utility of HHG system for materials characterization and lithographic processes for resist screening as the semiconductor industry transitions to high-NA EUV lithography.

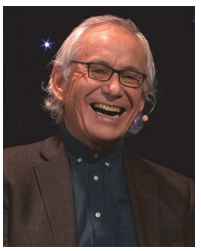

John Petersen is a principal scientist in the advanced patterning group at Imec and is the co-originator and coleader of Imec's AttoLab, the first industrial ultrafast dynamics laboratory of its type that is chartered for the development of spatio-temporal metrologies needed for the production of sub-3-nm nanoelectronics and nanophotonic devices and to emulate high-numerical-aperture extreme-ultraviolet imaging of photoresists. Concurrently, Petersen is an adjunct professor of physical chemistry at the University of Maryland, where he is developing resist materials and exposure technology for super-resolution lithography using two-way and three-way molecular switches as photoinitiators. John is a SPIE Fellow and a former Fellow at SEMATECH. Since 1980, John has been at the forefront of the development of lithography for the fabrication of semiconductor devices, where he continues to research the interplay between the physics and the chemistry of the photoresist imaging process. Petersen has worked at Texas Instruments, Shipley Company, Shipley Microelectronics, SEMATECH, Petersen Advanced Lithography, Periodic Structures, and now imec, Leuven, Belgium. He has published more than 80 papers, 45 of them as lead author/researcher, and he won the SEMI 2006 Innovation Award.